HOKKAIDO UNIVERSITY

Title	Symmetry-adapted modeling for molecules and crystals
Author(s)	Kusunose, Hiroaki; Oiwa, Rikuto; Hayami, Satoru
Citation	Physical Review B, 107(19), 195118-1-195118-14 https://doi.org/10.1103/PhysRevB.107.195118
Issue Date	2023
Doc URL	http://hdl.handle.net/2115/90132
Rights	©2023 American Physical Society　(Physical Review B Vol.107(19) 195118 2023)
Type	article
File Information	PhysRevB.107.195118-2.pdf

Instructions for use

Symmetry-adapted modeling for molecules and crystals

Hiroaki Kusunose [1] Rikuto Oiwa [1] and Satoru Hayami [2]

[1]*Department of Physics, Meiji University, Kawasaki 214-8571, Japan*
[2]*Graduate School of Science, Hokkaido University, Sapporo 060-0810, Japan*

We have developed a symmetry-adapted modeling procedure for molecules and crystals. By using the completeness of multipoles to express spatial and time-reversal parity-specific anisotropic distributions, we can generate systematically the complete symmetry-adapted multipole basis set to describe any of electronic degrees of freedom in isolated cluster systems and periodic crystals. The symmetry-adapted modeling is then achieved by expressing the Hamiltonian in terms of the linear combination of these bases belonging to the identity irreducible representation, and the model parameters (linear coefficients) in the Hamiltonian can be determined so as to reproduce the electronic structures given by the density-functional computation. We demonstrate our method for the modeling of graphene and emphasize usefulness of the symmetry-adapted basis to analyze and predict physical phenomena and spontaneous symmetry breaking in a phase transition. The present method is complementary to *de facto* standard Wannier tight-binding modeling, and it provides us with a fundamental basis to develop a symmetry-based analysis for materials science.

I. INTRODUCTION

Diversity is one of the fascinating aspects of materials science, and the diverse properties of materials are brought about by mutual interplay among electronic degrees of freedom, such as charge, atomic orbital and spin, and underlying molecular or crystal structure. Moreover, intriguing phenomena emerge by phase transitions with spontaneous symmetry breaking. In particular, order parameters of spin-orbital-lattice composite objects bring about various off-diagonal responses and generate nontrivial transport involving atomic internal objects.

In order to analyze proper material properties and predict bright new phenomena quantitatively, one needs microscopic modeling of materials. For such a purpose, the density-functional (DF) theory and related modelings have been widely used [1–6]. Once a tractable model is obtained, one uses it to discuss various response functions and to give a starting point for taking account of many-body effects such as electron correlations and electron-phonon interactions.

The Wannier-based tight-binding (Wannier TB) modeling from DF theory is the *de facto* standard, and there are several advantages, such as no need for electronic band fitting to a certain model, capturing covalent-bond feature of wave functions, and so on [7–9]. Nevertheless, there are several drawbacks as follows: (1) the obtained Wannier TB model does not satisfy the symmetry of a system rigorously due to a disentangling procedure of bands within a given energy window in addition to simple numerical errors; (2) as the Wannier basis functions differ from atomic orbital ones in general, representation matrices for physical quantities such as the orbital angular-momentum operator become unclear with respect to those bases; and (3) there are considerably small long-range hopping matrices in the Wannier TB model; however, it is quite cumbersome to neglect them without

losing the symmetry, which hampers us to compactify the Wannier TB model.

In this paper, we propose a complementary modeling procedure to overcome the above drawbacks, which fully respects the symmetry of a system, and atomic (internal) degrees of freedom, in its construction process. According to Neumann's principle, any macroscopic responses are characterized by point-group symmetry [10], and in the Landau theory of phase transition, nontrivial irreducible representation determines the fate of an emerging phase in which the order parameter is a macroscopic quantum-mechanical average of a microscopic degree of freedom [11]. Therefore, a seamless description between macroscopic quantities and microscopic degrees of freedom in accordance with symmetry is indispensable in a promising modeling method.

Realistic materials are characterized by anisotropic distributions in molecular or crystal structure in addition to spatial and time-reversal parities compatible with their symmetry. The symmetry-adapted multipoles in point group are suitable candidates to describe such parity-specific anisotropic distributions [12–14], as they have the completeness in angular space [15]. By utilizing the completeness of the multipoles, we construct the symmetry-adapted basis to describe any of electronic degrees of freedom in isolated cluster systems (e.g., molecules and quantum dots) and periodic crystals. Since the present multipole basis can treat the internal atomic degrees of freedom and molecular or crystal structures separately, it is able to bridge explicitly between macroscopic quantities and microscopic degrees of freedom. Indeed, various physical quantities appearing in ordinary Hamiltonians can be expressed by the multipole basis, whose examples are summarized in Table I.

Then symmetry-adapted modeling is achieved by expressing the Hamiltonian in terms of the linear combination of these bases belonging to the identity irreducible

TABLE I. Correspondence between physical quantities and symmetry-adapted multipole basis (SAMB). The upper, middle, and lower panels represent one-body, two-body, and hopping terms, respectively. The site (bond) dependence in the upper (middle) panel is expressed by the site cluster $\mathbb{Q}_{lm}^{(s)}$ (bond cluster $\mathbb{Q}_{lm}^{(b)}$, $\mathbb{T}_{lm}^{(b)}$) SAMBs. DM int. is the Dzyaloshinsky-Moriya interaction. The repeated indices are implicitly summed in the expression. The detailed meaning of these symbols will be explained in the main sections.

Type	Expression	Correspondence
Electric potential	ϕq	$q \rightarrow \mathbb{Q}_{0,0}^{(a)}$
Crystal field	$\phi_{lm} Q_{lm}$	$Q_{lm} \rightarrow \mathbb{Q}_{lm}^{(a)}$
Zeeman term	$-h^a m^a$	$m^a \rightarrow \mathbb{M}_{1m}^{(a)}$
Spin-orbit int.	$\zeta l^a \sigma^a$	$l^a, \sigma^a \rightarrow \mathbb{M}_{1m}^{(a)}$
Density-density int.	$V_{ij} n_i n_j$	$n_i n_j \rightarrow \mathbb{Q}_{0,0}^{(a)}$
Elastic energy	$\epsilon_{ij}^{ab} u_i^a u_j^b$	$u_i^a u_j^b \rightarrow \mathbb{Q}_{0,0}^{(a)}, \mathbb{Q}_{2m}^{(a)}$
Exchange int.	$J_{ij}^{ab} S_i^a S_j^b$	$S_i^a S_j^b \rightarrow \mathbb{Q}_{0,0}^{(a)}, \mathbb{Q}_{2m}^{(a)}$
DM int.	$D_{ij}^c \epsilon_{abc} S_i^a S_j^b$	$\epsilon_{abc} S_i^a S_j^b \rightarrow \mathbb{G}_{lm}^{(a)}$
Real hopping	$t_{ij} c_i^\dagger c_j + $ H.c.	$c_i^\dagger c_j + $ H.c. $\rightarrow \mathbb{Q}_{lm}^{(b)}$
Imaginary hopping	$\mathrm{i} t_{ij} c_i^\dagger c_j + $ H.c.	$\mathrm{i} c_i^\dagger c_j + $ H.c. $\rightarrow \mathbb{T}_{lm}^{(b)}$

representation. Once a symmetry-adapted model is constructed, one optimizes the model parameters (linear coefficients) to reproduce the electronic states given by DF computation. The optimization can be carried out by using the machine-learning technique with the deep neural network [16] having extremely low dependencies of initial guess. There have been several attempts to construct the TB Hamiltonian [17,18] based on machine-learning technique [19,20]. The TB models generated by Wang *et al.* [20] successfully reproduce the DF band dispersions with high accuracy, where the symmetry of the system is not considered and each hopping is regarded as a neuron in their neural network. On the other hand, in our scheme each symmetry-adapted multipole basis (SAMB) is a neuron in the neural network, and hence the symmetry is always maintained during the optimization process. We give the prime example of the basis construction and optimization by using graphene, and other examples are given in the Supplemental Material [21].

This paper is organized as follows: In Sec. II, we explain the construction procedure for the complete SAMB set. We first treat the case of isolated cluster systems by using an example of a fictitious molecule in C_{3v} point group, and then the case of periodic crystals is discussed. After setting up the general basis construction procedure, we give an application of our method to graphene in Sec. III. We construct the symmetry-adapted TB model for graphene up to sixth-neighbor hoppings and optimize the model parameters to reproduce DF energy dispersion. The final section summarizes the paper.

II. SYMMETRY-ADAPTED MULTIPOLE BASIS

In order to perform symmetry-adapted modeling, we introduce the complete orthonormal basis set that is classified according to the point-group symmetry. Such a basis set is
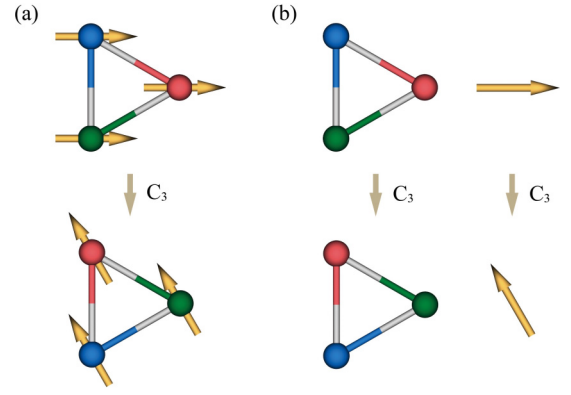

FIG. 1. Separation of the symmetry operation, C_3; (a) without separation and (b) operations separately to atomic sites/bonds and atomic degrees of freedom, e.g., spins.

called SAMB, in which any anisotropy is described by means of multipolar anisotropy [22]. Let us first discuss the SAMB in the case of isolated cluster systems such as molecules and quantum dots in Sec. II A. Then the case of periodic crystals is explained in Sec. II B. The conversions to full matrix form and momentum-space representation for a specified system are discussed in Sec. II C.

A. Isolated cluster systems

We begin with an isolated cluster system which consists of several atoms having internal degrees of freedom, i.e., atomic orbitals and spins, at each atomic site. Hereafter, we simply call the atomic orbitals including spins as "atomic orbitals." In general, the symmetry operations of the system can be applied separately to positions of atoms and atomic degrees of freedom as shown in Fig. 1. Because of this separable property, we can construct the SAMB separately for atomic sites/bonds and atomic degrees of freedom as follows.

1. Site cluster and bond cluster

First, we explain the SAMB for atomic sites and bonds. Let us choose a representative atomic site in the isolated cluster, and its position is $\boldsymbol{R}_1$. Then, a set of sites $(\boldsymbol{R}_1', \boldsymbol{R}_2', \ldots, \boldsymbol{R}_{N_g}')$ is obtained by applying the symmetry operation $\mathcal{G}_g$ in the point group as $\boldsymbol{R}_g' = \mathcal{G}_g \boldsymbol{R}_1$ ($g = 1, 2, \ldots, N_g$; $\mathcal{G}_1$ is assumed to be the identity operation), where N_g is the number of symmetry operations. Since some of the obtained sites are overlapped unless the sites belong to the general point, the total number of cluster sites N_s is less than N_g, and it is equivalent to the number in the Wyckoff symbol. We call the set of sites without duplication $(\boldsymbol{R}_1, \boldsymbol{R}_2, \ldots, \boldsymbol{R}_{N_s})$ "site cluster," and the one-to-many correspondence is expressed by $g(i)$ so as to satisfy $\boldsymbol{R}_i = \boldsymbol{R}_{g(i)}'$ ($i = 1, 2, \ldots, N_s$). All the sites in the isolated cluster system can be divided into a set of site clusters. For example, the division of site clusters in C_{3v} (31m) point group with $N_g = 6$ and $N_s = 3$ is shown by different colored spheres in Fig. 2.

Similarly, the bond cluster is obtained by applying the symmetry operation to a representative bond, $\boldsymbol{b}_1 @ \boldsymbol{c}_1$, where we have introduced the bond-vector $\boldsymbol{b}_1 = \boldsymbol{R}_{\mathrm{head}} - \boldsymbol{R}_{\mathrm{tail}}$ and the bond center $\boldsymbol{c}_1 = (\boldsymbol{R}_{\mathrm{head}} + \boldsymbol{R}_{\mathrm{tail}})/2$. The obtained bonds

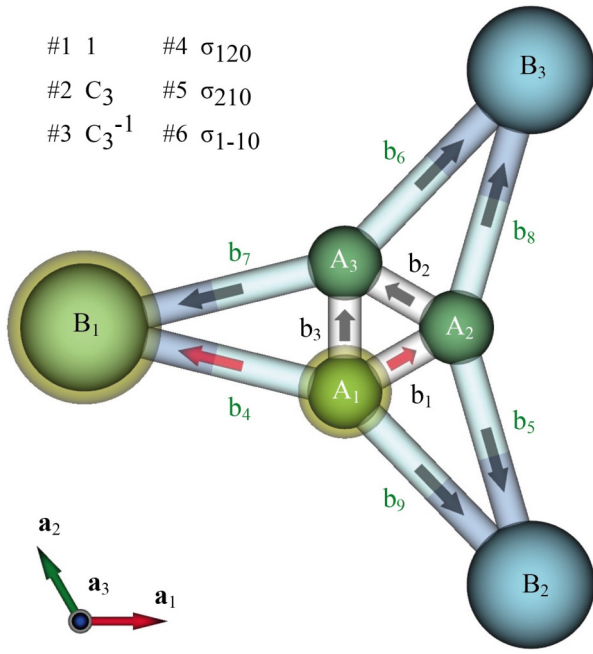| #1 | 1 | #4 | σ_{120} |
| #2 | C_3 | #5 | σ_{210} |
| #3 | C_3^{-1} | #6 | $\sigma_{1\text{-}10}$ |

FIG. 2. Example of site clusters (different colored spheres) and bond clusters (different colored bonds) in the C_{3v} (31m) point group (vertical mirrors in xz and equivalent planes). The representative site and bond are denoted by a yellow circle and red arrow, respectively. The trigonal units are $\boldsymbol{a}_1 = (1, 0, 0)$, $\boldsymbol{a}_2 = (-1/2, \sqrt{3}/2, 0)$, and $\boldsymbol{a}_3 = (0, 0, 1)$.

$(\boldsymbol{b}_1'@\boldsymbol{c}_1', \boldsymbol{b}_2'@\boldsymbol{c}_2', \cdots, \boldsymbol{b}_{N_g}'@\boldsymbol{c}_{N_g}')$ are duplicated in general with the equivalent bond centers. Then the set of bonds without duplication $(\boldsymbol{b}_1@\boldsymbol{c}_1, \boldsymbol{b}_2@\boldsymbol{c}_2, \cdots, \boldsymbol{b}_{N_b}@\boldsymbol{c}_{N_b})$ constitutes the "bond cluster," where N_b is the number of bonds in the bond cluster. In contrast to the site cluster, some bonds may coincide with other bond with reversed direction. In this case, we attach a negative sign to the symmetry operation in the correspondence $g(i)$, i.e., the one-to-many correspondence is given by $g(i)$ with $\boldsymbol{c}_i = \boldsymbol{c}_{|g(i)|}'$ and $\boldsymbol{b}_i = \text{sgn}[g(i)]\boldsymbol{b}_{|g(i)|}'$. All the bonds in the isolated cluster system can be divided into a set of bond clusters, as shown by different colored bonds in Fig. 2. The one-to-many correspondences of the site/bond clusters for the example of the fictitious molecule in Fig. 2 are shown in Table II.

2. Symmetry-adapted multipole basis

Once the site and bond clusters are introduced, we are ready to construct the SAMB for each cluster. Let us begin with the SAMB for a site cluster, which enables us to express any site-dependent quantity in a cluster. To this end, we introduce the normalized spherical harmonics defined by

$$O_{lm}(\boldsymbol{r}) = r^l \sqrt{\frac{4\pi}{2l+1}} Y_{lm}(\hat{\boldsymbol{r}}), \qquad (1)$$

where $r = |\boldsymbol{r}|$, $\hat{\boldsymbol{r}} = \boldsymbol{r}/r$, and the spherical harmonics, $Y_{lm}(\hat{\boldsymbol{r}})$ with the rank $l (= 0, 1, 2, \dots)$ and component $m (= -l, -l + 1, \dots, l)$. Since the point group is a subgroup of the rotation group supplemented by the inversion operation, we use symmetry-adapted harmonics $O_{l\xi}(\boldsymbol{r})$ ($\xi = (\Gamma, n, \gamma)$) instead

TABLE II. One-to-many correspondences in the site/bond clusters for the example in Fig. 2, in which $x = 1/6$ and $x' = 2/3$ are used.

Site A	$\boldsymbol{R}_i$	$g(i)$	Site B	$\boldsymbol{R}_i$	$g(i)$
A_1	$[-x, -x, 0]$	$[1,6]$	B_1	$[-x', 0, 0]$	$[1,4]$
A_2	$[x, 0, 0]$	$[2,5]$	B_2	$[0, -x', 0]$	$[2,6]$
A_3	$[0, x, 0]$	$[3,4]$	B_3	$[x', x'0]$	$[3,5]$
Bond A $\rightarrow$ A		$\boldsymbol{b}_i@\boldsymbol{c}_i$			$g(i)$
b_1		$\left[\frac{1}{3}, \frac{1}{6}, 0\right]@\left[0, -\frac{1}{12}, 0\right]$			$[1,\text{-}5]$
b_2		$\left[-\frac{1}{6}, \frac{1}{6}, 0\right]@\left[\frac{1}{12}, \frac{1}{12}, 0\right]$			$[2,\text{-}4]$
b_3		$\left[\frac{1}{6}, \frac{1}{3}, 0\right]@\left[-\frac{1}{12}, 0, 0\right]$			$[\text{-}3,6]$
Bond A $\rightarrow$ B		$\boldsymbol{b}_i@\boldsymbol{c}_i$			$g(i)$
b_4		$\left[-\frac{1}{2}, \frac{1}{6}, 0\right]@\left[-\frac{5}{12}, -\frac{1}{12}, 0\right]$			$[1]$
b_5		$\left[-\frac{1}{6}, -\frac{2}{3}, 0\right]@\left[\frac{1}{12}, -\frac{1}{3}, 0\right]$			$[2]$
b_6		$\left[\frac{2}{3}, \frac{1}{2}, 0\right]@\left[\frac{1}{3}, \frac{5}{12}, 0\right]$			$[3]$
b_7		$\left[-\frac{2}{3}, -\frac{1}{6}, 0\right]@\left[-\frac{1}{3}, \frac{1}{12}, 0\right]$			$[4]$
b_8		$\left[\frac{1}{2}, \frac{2}{3}, 0\right]@\left[\frac{5}{12}, \frac{1}{3}, 0\right]$			$[5]$
b_9		$\left[\frac{1}{6}, -\frac{1}{2}, 0\right]@\left[-\frac{1}{12}, -\frac{5}{12}, 0\right]$			$[6]$

of $O_{lm}(\boldsymbol{r})$ by appropriate linear combination as

$$O_{l\xi}(\boldsymbol{r}) = \sum_m U_{m,\xi}^{(l)} O_{lm}(\boldsymbol{r}), \qquad (2)$$

where $U_{m,\xi}^{(l)}$ is a matrix element of the unitary matrix for basis transformation and Γ and γ represent the irreducible representation (irrep.) and its component, respectively. The label n is the multiplicity to distinguish independent harmonics belonging to the same irrep. It should be noted that the harmonics in each irrep., especially for two- and three-dimensional ones, must be defined so as to give equivalent representation matrices for all symmetry operations. For example, the harmonics up to rank 3 in the C_{3v} (3m1) point group are given in Table III (they are also used for D_{6h} for later purposes). For point groups with complex characters, i.e., E_a ($x + iy$ like) and E_b ($x - iy$ like), we treat them together as E irrep. by hermiting as $[O_{l,(E_a,n)} + O_{l,(E_b,n)}]/\sqrt{2}$ and $[O_{l,(E_a,n)} - O_{l,(E_b,n)}]/\sqrt{2}i$.

With this preliminary, the SAMB for a site cluster is obtained by evaluating $O_{l\xi}(\boldsymbol{r})$ at $\boldsymbol{r} = \boldsymbol{R}_i$ in the site cluster, i.e., we obtain the N_s-dimensional vector basis as

$$\mathbb{Q}_{l\xi}^{(s)} = \left(q_1^{(l\xi)}, q_2^{(l\xi)}, \dots, q_{N_s}^{(l\xi)}\right), \quad q_i^{(l\xi)} = O_{l\xi}(\boldsymbol{R}_i), \quad (3)$$

where the black-board font is used to represent the orthonormal basis and "Q" denotes the electric multipole indicating that it has an electric polar tensor property. The superscript "(s)" indicates the SAMB for the site cluster. We construct the SAMBs from the lowest rank as $l = 0, 1, 2, \dots$, until N_s-independent bases are obtained. When the obtained SAMBs are not orthonormalized, we use the Gram-Schmidt method to orthonormalize them. The obtained SAMBs are equivalent to the ordinary molecular orbitals consisting of spinless atomic s orbitals at each site.

TABLE III. Harmonics up to rank 3 in C_{3v} (31m) point group. The labels in the square bracket represent those for D_{6h} point group. The label g and u are exchanged in the irrep. of the axial vector in D_{6h}.

l	Γ	n	γ	Form	Axial
0	$A_1 [A_{1g}]$	–	–	1	
1	$A_1 [A_{2u}]$	–	–	z	Z
	$E [E_{1u}]$	–	u	x	$-Y$
			v	y	X
2	$A_1 [A_{1g}]$	–	–	$\frac{1}{2}(3z^2 - r^2)$	
	$E [E_{1g}]$	1 [-]	u	$\sqrt{3}xz$	
			v	$\sqrt{3}yz$	
	$E [E_{2g}]$	2 [-]	u	$\frac{\sqrt{3}}{2}(x^2 - y^2)$	
			v	$-\sqrt{3}xy$	
3	$A_1 [A_{2u}]$	1 [-]	–	$\frac{1}{2}z(5z^2 - 3r^2)$	
	$A_1 [B_{2u}]$	2 [-]	–	$\frac{\sqrt{10}}{4}x(x^2 - 3y^2)$	
	$A_2 [B_{1u}]$	–	–	$\frac{\sqrt{10}}{4}y(3x^2 - y^2)$	
	$E [E_{1u}]$	1 [-]	u	$\frac{\sqrt{6}}{4}x(5z^2 - r^2)$	
			v	$\frac{\sqrt{6}}{4}y(5z^2 - r^2)$	
	$E [E_{2u}]$	2 [-]	u	$\frac{\sqrt{15}}{2}z(x^2 - y^2)$	
			v	$-\sqrt{15}xyz$	

3. Virtual cluster and mapping to original cluster

Similarly to the case of the site cluster, the SAMB may be constructed for a bond cluster by evaluating $O_{l\xi}(\boldsymbol{r})$ at the bond center $\boldsymbol{r} = \boldsymbol{c}_i$. However, there is a difficulty that $O_{l\xi}(\boldsymbol{r})$ sometimes gives useless results when a position of a bond center becomes the origin. Moreover, in periodic crystals, as discussed later, there is an ambiguity of the choice of the origin in a cluster. There is an additional difficulty in the nonsymmorphic space group, i.e., position vectors of the symmetry-equivalent sites in a cluster have different distances from the origin whatever we choose. These difficulties hamper us to construct the SAMB based on the spherical harmonics.

To avoid these difficulties, we introduce the virtual cluster in which the virtual sites $(\boldsymbol{r}_1, \boldsymbol{r}_2, \ldots, \boldsymbol{r}_{N_g}; \boldsymbol{r}_1$ can be arbitrarily chosen) are given by the N_g (i.e., $N_s = N_g$) general points of the relevant point group [23]. Then, we construct the SAMB with respect to the sites in the virtual cluster (indicated by the overline) as

$$\overline{\mathbb{Q}}_{l\xi} = \left(v_1^{(l\xi)}, v_2^{(l\xi)}, \ldots, v_{N_g}^{(l\xi)}\right), \quad v_g^{(l\xi)} = O_{l\xi}(\boldsymbol{r}_g). \quad (4)$$

Note that the SAMB in the virtual cluster can be prepared in advance for 32 crystallographic point groups as they are independent from an original cluster. For example, the orthonormalized SAMB in the virtual cluster of the C_{3v} (3m1) point group is summarized in Table IV, in which the sites $\{\boldsymbol{r}_g\}$ are generated by the representative point, $\boldsymbol{r}_1 = (1, -1, 0)$.

Once we obtain a set of the SAMBs, $\{\overline{\mathbb{Q}}_{l\xi}\}$, the SAMB for the original site cluster can be obtained by mapping the virtual

TABLE IV. Orthonormalized SAMB in the virtual cluster of C_{3v} (31m). The cluster sites in the trigonal unit are given by $\{\boldsymbol{r}_g\} = \{(1, -1, 0), (1, 2, 0), (-2, -1, 0), (2, 1, 0), (-1, -2, 0), (-1, 1, 0)\}$. The indices (l, Γ, n, γ) correspond to those in Table III.

No.	l	Γ	n	γ	$\overline{\mathbb{Q}}_{l\xi}$
1	0	A_1	–	–	$\frac{1}{\sqrt{6}}(1, 1, 1, 1, 1, 1)$
2	1	E	–	u	$\frac{1}{2}(1, 0, -1, 1, 0, -1)$
3				v	$\frac{1}{2\sqrt{3}}(-1, 2, -1, 1, -2, 1)$
4	2	E	2	u	$\frac{1}{2\sqrt{3}}(1, -2, 1, 1, -2, 1)$
5				v	$\frac{1}{2}(1, 0, -1, -1, 0, 1)$
6	3	A_2	–	–	$\frac{1}{\sqrt{6}}(-1, -1, -1, 1, 1, 1)$

cluster elements onto the original site cluster ones as

$$\mathbb{Q}_{l\xi}^{(s)} = \left(q_1^{(l\xi)}, q_2^{(l\xi)}, \ldots, q_{N_c}^{(l\xi)}\right), \quad q_i^{(l\xi)} = \sum_g^{g(i)} v_g^{(l\xi)}, \quad (5)$$

where the one-to-many correspondence (mapping) $g(i)$ is determined for the original site cluster.

Although the SAMB for an original bond cluster can be obtained in a similar way, we need special care for the bond direction. When we express a symmetric-bond dependence such as a real hopping, e.g., $(c_i^\dagger c_j + c_j^\dagger c_i)$, we can omit the directional property of bonds. In this case, we construct the SAMB for a bond cluster in the same way as a site cluster as

$$\mathbb{Q}_{l\xi}^{(b)} = \left(c_1^{(l\xi)}, c_2^{(l\xi)}, \cdots, c_{N_b}^{(l\xi)}\right), \quad c_i^{(l\xi)} = \sum_g^{g(i)} v_g^{(l\xi)}, \quad (6)$$

where the mapping $g(i)$ is determined for the original N_b bond cluster, and the superscript "(b)" indicates the SAMB for the bond cluster.

On the other hand, when we consider an antisymmetric bond dependence such as an imaginary hopping, e.g., $i(c_i^\dagger c_j - c_j^\dagger c_i)$, the directional property must be taken into account. In this case, the SAMB for a bond cluster is given as

$$\mathbb{T}_{l\xi}^{(b)} = i\left(b_1^{(l\xi)}, b_2^{(l\xi)}, \cdots, b_{N_b}^{(l\xi)}\right), \quad b_i^{(l\xi)} = \sum_g^{g(i)} \text{sgn}[g] v_{|g|}^{(l\xi)}, \quad (7)$$

in order to satisfy the antisymmetric property of the bonds. Here we have attached the phase factor i for later convenience. The real $\mathbb{Q}_{l\xi}^{(b)}$ and imaginary $\mathbb{T}_{l\xi}^{(b)}$ SAMBs are always orthogonal to each other. "T" denotes the magnetic-toroidal multipole, indicating that it has a magnetic polar tensor property. The SAMB for the site/bond clusters in the case of the example shown in Fig. 2 is summarized in Table V.

As explained the above, we can construct a set of the SAMBs for the original site and bond clusters in terms of the polar tensors, $\mathbb{Q}_{l\xi}^{(b)}$ and $\mathbb{T}_{l\xi}^{(b)}$. When the obtained SAMBs are not orthonormalized, we again use the Gram-Schmidt method. The symbol $\mathbb{Y}_{l\xi}$ is used to refer to $\mathbb{Q}_{l\xi}^{(s)}$, $\mathbb{Q}_{l\xi}^{(b)}$, or $\mathbb{T}_{l\xi}^{(b)}$ in the site/bond clusters, and we call them "cluster SAMB."

TABLE V. Orthonormalized SAMB for the example site/bond clusters shown in Fig. 2. The Q-type SAMB for A $\rightarrow$ B bond cluster is the same as that for the virtual cluster in Table IV, while T-type is given by that multiplied by the phase factor i. The indices (l, Γ, n, γ) correspond to those in Table III.

l	Γ	n	γ	$\mathbb{Q}^{(s)}_{l\xi}$ for A	l	Γ	n	γ	$\mathbb{Q}^{(s)}_{l\xi}$ for B
0	A_1	–	–	$\frac{1}{\sqrt{3}}(1,1,1)$	0	A_1	–	–	$\frac{1}{\sqrt{3}}(1,1,1)$
2	E	2	u	$\frac{1}{\sqrt{6}}(1,-2,1)$	1	E	–	u	$\frac{1}{\sqrt{6}}(2,-1,-1)$
			v	$\frac{1}{\sqrt{2}}(1,0,-1)$				v	$\frac{1}{\sqrt{2}}(0,1,-1)$

l	Γ	n	γ	$\mathbb{Q}^{(b)}_{l\xi}$ for A $\rightarrow$ A	l	Γ	n	γ	$\mathbb{T}^{(b)}_{l\xi}$ for A $\rightarrow$ A
0	A_1	–	–	$\frac{1}{\sqrt{3}}(1,1,1)$	3	A_2	–	–	$\frac{i}{\sqrt{3}}(-1,-1,1)$
1	E	–	u	$\frac{1}{\sqrt{6}}(1,1,-2)$	1	E	–	u	$\frac{i}{\sqrt{2}}(1,-1,0)$
			v	$\frac{1}{\sqrt{2}}(-1,1,0)$				v	$\frac{i}{\sqrt{6}}(1,1,2)$

4. SAMB for atomic degrees of freedom

Next, we consider the SAMB for atomic degrees of freedom, which we call "atomic SAMB." The complete set of the atomic SAMB has already been discussed in the literature [15], and they can be expressed in terms of electric (time-reversal even polar), magnetic (time-reversal odd axial), electric-toroidal (time-reversal even axial), and magnetic-toroidal (time-reversal odd polar) multipole bases, $\mathbb{Q}^{(a)}_{lm}$, $\mathbb{M}^{(a)}_{lm}$, $\mathbb{G}^{(a)}_{lm}$, and $\mathbb{T}^{(a)}_{lm}$ in the rotation group. The superscript "(a)" indicates the atomic SAMB. The symbol $\mathbb{X}_{lm}$ is used to refer to all of the four-type atomic SAMBs.

The spinful atomic SAMB can be obtained by the direct product of the spinless atomic SAMB $\mathbb{X}^{(orb)}_{lm}$ and identity and Pauli matrices σ_{sn} ($\sigma_{00} = \sigma_0$, $\sigma_{10} = \sigma_z$, $\sigma_{1\pm 1} = \mp(\sigma_x \pm i\sigma_y)/\sqrt{2}$) by using the addition rule of the angular momentum as

$$\mathbb{X}_{lm}(s,k) = i^{s+k} \sum_n \langle l+k, m-n; sn|lm\rangle \mathbb{X}^{(orb)}_{l+k,m-n}\sigma_{sn}, \quad (8)$$

where $\langle l_1, m_1; l_2, m_2|lm\rangle$ is the Clebsch-Gordan (CG) coefficient. See Ref. [15] for the expression of $\mathbb{X}^{(orb)}_{lm}$. Note that $\mathbb{X}_{lm}(0,0) = \mathbb{X}^{(orb)}_{lm}\sigma_0$.

In evaluating the matrix elements of $\mathbb{X}_{lm}$, the orbital angular momentum of the bra and ket states can be different. For instance, when we consider an electron hopping from s orbital in A site to p_x orbital in B site and vice versa, s-p_x off-diagonal Hilbert space must be taken into account. It should be emphasized that $\mathbb{X}_{lm}(s,k)$ must be treated independently between different (e.g., $\langle s|s\rangle$, $\langle p|p\rangle$, and $\langle s|p\rangle$) Hilbert spaces, even if all the indices (X, l, m, s, k) are the same.

The atomic SAMB for point group can be obtained by means of the unitary matrix in Eq. (2) as

$$\mathbb{X}_{l\xi,sk} = \sum_m U^{(l)}_{m,\xi} \mathbb{X}_{lm}(s,k). \quad (9)$$

The formula to compute the matrix elements of $\mathbb{X}_{lm}(s,k)$ is summarized in Ref. [15], and those of $\mathbb{X}_{l\xi,sk}$ for point group can be obtained by the appropriate unitary transformation, $U^{(l)}_{m,\xi}$ as well. Then $\mathbb{X}_{l\xi,sk}$ can be normalized straightforwardly. The example of expressions of $\mathbb{X}_{l\xi} = \mathbb{X}_{l\xi,00}$ is given in Table VI, where the spinless s orbital (p orbitals) are assumed at A (B) sites.

5. Combined SAMB for atomic and site/bond cluster

In the previous subsections, we have constructed the complete orthonormal SAMBs for the atomic degrees of freedom $\mathbb{X}_{l\xi,sk}$ and for the site/bond clusters, $\mathbb{Y}_{l\xi}$. Here we construct the SAMB by performing the irreducible decomposition of the direct product of these two SAMBs.

To this end, we begin with the addition rule of the spherical harmonic-like functions,

$$Z_{lm} = (-i)^{l_1+l_2-l} \sum_{m_1m_2} \langle l_1m_1, l_2m_2|lm\rangle X_{l_1m_1} Y_{l_2m_2}, \quad (10)$$

where X_{lm} transforms like the spherical harmonics $Y_{lm}(\hat{r})$ against a spatial rotation and satisfies $X^\dagger_{lm} = (-1)^m X_{l-m}$. Y_{lm} and Z_{lm} have the same properties as X_{lm}. The phase factor has been introduced to satisfy $Z^\dagger_{lm} = Z_{l-m}$.

By considering consistency for the spatial and time-reversal parities, they must coincide with each other in both sides of Eq. (10). For the time-reversal parity, we introduce the time-reversal parity as a function of multipole type as

$$t(Q) = t(G) = +1, \quad t(T) = t(M) = -1, \quad (11)$$

where $+1$ and -1 denote the time-reversal even and odd, respectively. Then the time-reversal selection rule is given by $\delta[t(X)t(Y), t(Z)]$, where $\delta[a,b]$ is the Kronecker's delta.

Similarly, we introduce the spatial parity function as

$$p(Q) = p(T) = 0, \quad p(G) = p(M) = 1, \quad (12)$$

where 0 and 1 denote polar and axial, respectively. Equation (10) has finite value only for $|l_1 - l_2| \leqslant l \leqslant l_1 + l_2$, and when the difference between $l_1 + l_2$ and l is odd, the spatial parity of Z becomes opposite to that of the product of X and Y. Hence, the spatial parity selection rule reads

$$\delta[(l_1 + l_2 - l + p(X) + p(Y) - p(Z)) \bmod 2, 0]. \quad (13)$$

By these considerations, we obtain the extended addition rule as

$$\hat{\mathbb{Z}}_{lm}(s,k) = \sum_{m_1m_2} C^{l_1m_1, l_2m_2}_{lm}(X,Y|Z) \, \mathbb{X}_{l_1m_1}(s,k) \otimes \mathbb{Y}_{l_2m_2}, \quad (14)$$

with the "CG" coefficient,

$$C^{l_1m_1, l_2m_2}_{lm}(X,Y|Z)$$
$$= (-i)^{l_1+l_2-l} \langle l_1m_1, l_2m_2|lm\rangle \Delta^{l_1,l_2}_l(X,Y|Z), \quad (15)$$

TABLE VI. Orthonormalized atomic SAMB. We consider the spinless s orbital in A sites, while $(p_x, p_y; p_z)$ orbitals in B sites in the example of Fig. 2. Note that p_x, p_y (p_z) belong to E (A_1) irrep. As only $s = k = 0$ (charge sector) SAMBs are active in the spinless Hilbert space, we omit (s, k). In $\langle s|s \rangle$ Hilbert space, there is only $\mathbb{Q}_{0,A_1} = (1)$. In $\langle s|p \rangle$ Hilbert space, $\mathbb{T}_{l\xi}^{(a)}$ is given by multiplying $\mathbb{Q}_{l\xi}^{(a)}$ by the phase factor i. The indices (l, Γ, n, γ) correspond to those in Table III.

l	Γ	n	γ	$\mathbb{Q}_{l\xi}^{(a)}$ for $\langle p|p \rangle$	l	Γ	n	γ	$\mathbb{Q}_{l\xi}^{(a)}$ for $\langle p|p \rangle$
0	A_1	–	–	$\frac{1}{\sqrt{3}}\begin{pmatrix} 1 & 0 & 0 \\ 0 & 1 & 0 \\ 0 & 0 & 1 \end{pmatrix}$	2	A_1	–	–	$\frac{1}{\sqrt{6}}\begin{pmatrix} -1 & 0 & 0 \\ 0 & -1 & 0 \\ 0 & 0 & 2 \end{pmatrix}$
2	E	1	u	$\frac{1}{\sqrt{2}}\begin{pmatrix} 0 & 0 & 1 \\ 0 & 0 & 0 \\ 1 & 0 & 0 \end{pmatrix}$	2	E	2	u	$\frac{1}{\sqrt{2}}\begin{pmatrix} 1 & 0 & 0 \\ 0 & -1 & 0 \\ 0 & 0 & 0 \end{pmatrix}$
			v	$\frac{1}{\sqrt{2}}\begin{pmatrix} 0 & 0 & 0 \\ 0 & 0 & 1 \\ 0 & 1 & 0 \end{pmatrix}$				v	$-\frac{1}{\sqrt{2}}\begin{pmatrix} 0 & 1 & 0 \\ 1 & 0 & 0 \\ 0 & 0 & 0 \end{pmatrix}$

l	Γ	n	γ	$\mathbb{M}_{l\xi}^{(a)}$ for $\langle p|p \rangle$	l	Γ	n	γ	$\mathbb{Q}_{l\xi}^{(a)}$ for $\langle s|p \rangle$
1	A_2	–	–	$\frac{1}{\sqrt{2}}\begin{pmatrix} 0 & -i & 0 \\ i & 0 & 0 \\ 0 & 0 & 0 \end{pmatrix}$	1	A_1	–	–	$(0 \quad 0 \quad 1)$
1	E	–	u	$\frac{1}{\sqrt{2}}\begin{pmatrix} 0 & 0 & -i \\ 0 & 0 & 0 \\ i & 0 & 0 \end{pmatrix}$	1	E	–	u	$(1 \quad 0 \quad 0)$
			v	$\frac{1}{\sqrt{2}}\begin{pmatrix} 0 & 0 & 0 \\ 0 & 0 & -i \\ 0 & i & 0 \end{pmatrix}$				v	$(0 \quad 1 \quad 0)$

and

$$\Delta_l^{l_1,l_2}(X, Y|Z) = \delta[t(X)t(Y), t(Z)]\delta[(l_1 + l_2 - l \\ + p(X) + p(Y) - p(Z)) \bmod 2, 0]. \quad (16)$$

Then, by the unitary transformation from the rotation group to point group, we finally obtain the combined SAMB as

$$\hat{\mathbb{Z}}_{l\xi,sk} = \sum_{\xi_1\xi_2} C_{l\xi}^{l_1\xi_1, l_2\xi_2}(X, Y|Z) \, \mathbb{X}_{l_1\xi_1,sk} \otimes \mathbb{Y}_{l_2\xi_2}, \quad (17)$$

where

$$C_{l\xi}^{l_1\xi_1, l_2\xi_2}(X, Y|Z) = \sum_{mm_1m_2} U_{m_1,\xi_1}^{(l_1)*} U_{m_2,\xi_2}^{(l_2)*} \\ \times C_{lm}^{l_1m_1, l_2m_2}(X, Y|Z) U_{m,\xi}^{(l)}. \quad (18)$$

If the obtained SAMBs are not orthonormalized, then the Gram-Schmidt method is applied. Since $\mathbb{X}_{l_1\xi_1,sk}$ and $\mathbb{Y}_{l_2\xi_2}$ are already orthonormalized, this is done by performing the Gram-Schmidt method only to the CG coefficients. The example of the combined SAMB for the case of Fig. 2 with the spinless s orbital (p orbitals) at A (B) sites is given in Table VII.

B. Periodic crystals

In this subsection, we discuss the SAMB, $\hat{\mathbb{Z}}_{l\xi,sk}$, for periodic crystals. The procedure is almost the same as that for isolated cluster systems described in the previous subsections. Since the atomic SAMB $\mathbb{X}_{l\xi,sk}$ is irrelevant either to isolated cluster systems or periodic crystals, we only consider the SAMB of the site/bond clusters, $\mathbb{Y}_{l\xi}$.

In periodic crystals, the site/bond cluster is defined in a similar manner as described in Sec. II A 1. Since there are translation operations, sites $\mathbf{R}_g'$ and bond centers $\mathbf{c}_g'$ must be shifted to the home unit cell in defining the site/bond cluster.

Then let us introduce the associated point group for space group in question. The associated point group is given by omitting the superscript of the space group in Schönflies notation, e.g., C_{3v} for C_{3v}^4 (#159, P31c), and its symmetry operations are given by those of the relevant space group without the (partial) translations. It should be noted that there is a one-to-one correspondence between the symmetry operations of the space group and those of its associated point group. Through this associated point group, we can determine the one-to-many correspondence $g(i)$ between the site/bond cluster in the periodic crystals and virtual cluster by means of the symmetry operations, g. Once we establish the one-to-many correspondence, we can construct the SAMB of the site/bond clusters $\mathbb{Y}_{l\xi}$, and hence the combined SAMB $\hat{\mathbb{Z}}_{l\xi,sk}$, in the same manner for isolated cluster systems. It should be emphasized that there is essentially no ambiguity about how to choose site/bond clusters and their origin by this prescription.

C. Full matrix form

In the previous subsections, we have explained how to construct the SAMB both for isolated cluster systems and periodic crystals. In general, the shapes of the obtained atomic SAMBs $\mathbb{X}_{l\xi,sk}$ are different from each other depending on the combination of the bra and ket states. Moreover, the dimensions of the SAMBs $\mathbb{Y}_{l\xi}$ are different among site/bond clusters. To obtain the full matrix form with respect to the total Hilbert space of the targeting system (see Fig. 3),

TABLE VII. Combined orthonormalized SAMBs belonging to the identity A_1 irrep. The abbreviation $[\mathbb{X} \otimes \mathbb{Y}] = (\mathbb{X}_u \otimes \mathbb{Y}_u + \mathbb{X}_v \otimes \mathbb{Y}_v)/\sqrt{2}$ is used for E irrep. As $\mathbb{Q}^{(a)}_{l\xi,sk}$ is spinless, $s = 0$ and $k = 0$ are omitted. The indices (l, Γ, n, γ) correspond to those in Table III.

l	Γ	n	γ	$\hat{\mathbb{Q}}_{l\xi}$ for A(s)	l	Γ	n	γ	$\hat{\mathbb{Q}}_{l\xi}$ for A(s) → A(s)
0	A_1	–	–	$\mathbb{Q}^{(a)}_{0,A_1} \otimes \mathbb{Q}^{(s)}_{0,A_1}$	0	A_1	–	–	$\mathbb{Q}^{(a)}_{0,A_1} \otimes \mathbb{Q}^{(b)}_{0,A_1}$

l	Γ	n	γ	$\hat{\mathbb{Q}}_{l\xi}$ for B(p)	l	Γ	n	γ	$\hat{\mathbb{Q}}_{l\xi}$ for A(s) → B(p)
0	A_1	–	–	$\mathbb{Q}^{(a)}_{0,A_1} \otimes \mathbb{Q}^{(s)}_{0,A_1}$	0	A_1	–	–	$\left[\mathbb{Q}^{(a)}_{1,E} \otimes \mathbb{Q}^{(b)}_{1,E}\right]$
1	A_1	–	–	$\left[\mathbb{Q}^{(a)}_{2,E,1} \otimes \mathbb{Q}^{(s)}_{1,E}\right]$	1	A_1	–	–	$\mathbb{Q}^{(a)}_{1,A_1} \otimes \mathbb{Q}^{(b)}_{0,A_1}$
2	A_1	–	–	$\mathbb{Q}^{(a)}_{2,A_1} \otimes \mathbb{Q}^{(s)}_{0,A_1}$	3	A_1	2	–	$\left[\mathbb{Q}^{(a)}_{1,E} \otimes \mathbb{Q}^{(b)}_{2,E,2}\right]$
3	A_1	2	–	$\left[\mathbb{Q}^{(a)}_{2,E,2} \otimes \mathbb{Q}^{(s)}_{1,E}\right]$					

we carry out the rearrangement of the basis elements, and Fourier transformation for periodic crystals, in the following procedure.

1. Conversion to full matrix form

For the atomic orbitals, we consider the direct sum of the Hilbert spaces of all the relevant atomic orbitals and assign each $\mathbb{X}_{l\xi,sk}$ for a given bra-ket states to an appropriate block of the matrix. Similarly, we consider the Hilbert space of all of the relevant sites in the targeting system and sum each element $[\mathbb{Y}_{l\xi}](i)$ to the appropriate matrix element in the case of isolated cluster systems.

On the other hand, for periodic crystals, we must use momentum-space representation. In order to transform the SAMB to the momentum space, we perform Fourier transformation for each bond in bond clusters. Namely, the ith component of the SAMB is transformed as

$$[\mathbb{Y}_{l\xi}](i) \rightarrow e^{-i\mathbf{k} \cdot \mathbf{b}_i}[\mathbb{Y}_{l\xi}](i). \tag{19}$$

Note that the complex conjugate of $e^{-i\mathbf{k}\cdot\mathbf{b}_i}[\mathbb{Y}_{l\xi}](i)$ is obtained by reverting the bond direction $\mathbf{b}_i \rightarrow -\mathbf{b}_i$, especially due to the phase factor i in $\mathbb{T}^{(b)}_{l\xi}$. The expression of the SAMB in site clusters does not change in the momentum space.

By the above procedure, we obtain the full matrix form of $\mathbb{Y}_{l\xi}$ or its momentum-space representation, which we denote as $\mathbb{Y}_{l\xi}(\mathbf{k})$. Then, the SAMB $\mathbb{Z}_{l\xi,sk}$ in the full matrix form is

obtained by

$$\hat{\mathbb{Z}}_{l\xi,sk} = \sum_{\xi_1\xi_2} C^{l_1\xi_1,l_2\xi_2}_{l\xi}(X, Y|Z)\, \mathbb{X}_{l_1\xi_1,sk} \otimes \mathbb{Y}_{l_2\xi_2}, \tag{20}$$

or

$$\hat{\mathbb{Z}}_{l\xi,sk}(\mathbf{k}) = \sum_{\xi_1\xi_2} C^{l_1\xi_1,l_2\xi_2}_{l\xi}(X, Y|Z)\, \mathbb{X}_{l_1\xi_1,sk} \otimes \mathbb{Y}_{l_2\xi_2}(\mathbf{k}). \tag{21}$$

Here the binary operator, $\otimes$, simply means the direct product of two Hermitian matrices, $\mathbb{X}_{l_1\xi_1,sk}$ and $\mathbb{Y}_{l_2\xi_2}$.

2. Conversion to structure-factor form

The Hermitian full matrix form of $\mathbb{Y}_{l_2\xi_2}(\mathbf{k})$ can be further decomposed into $\mathbf{k}$-independent "uniform matrix" basis $\mathbb{U}_{l\xi}$ and "structure factor" $\mathbb{F}_{l\xi}(\mathbf{k})$ as follows. Let us first introduce the momentum representation of $\mathbb{Q}^{(b)}_{l\xi}$ and $\mathbb{T}^{(b)}_{l\xi}$ as

$$\mathbb{Q}^{(k)}_{l\xi}(\mathbf{k}) \equiv \sqrt{2} \sum_i \cos(\mathbf{k} \cdot \mathbf{b}_i)\big[\mathbb{Q}^{(b)}_{l\xi}\big](i),$$

$$\mathbb{T}^{(k)}_{l\xi}(\mathbf{k}) \equiv -\sqrt{2}i \sum_i \sin(\mathbf{k} \cdot \mathbf{b}_i)\big[\mathbb{T}^{(b)}_{l\xi}\big](i). \tag{22}$$

Here $\mathbb{Q}^{(k)}_{l\xi}(\mathbf{k})$ and $\mathbb{T}^{(k)}_{l\xi}(\mathbf{k})$ are real functions and transformed as $O_{l\xi}(\mathbf{k})$ for the symmetry operations, and the time-reversal operation is $\mathcal{T}[\mathbb{Q}^{(k)}_{l\xi}(\mathbf{k})] = \mathbb{Q}^{(k)}_{l\xi}(-\mathbf{k})$ and $\mathcal{T}[\mathbb{T}^{(k)}_{l\xi}(\mathbf{k})] = -\mathbb{T}^{(k)}_{l\xi}(-\mathbf{k})$. We denote all of the symmetry-adapted structure factor ("structure SAMB") as $\mathbb{F}_{l\xi}(\mathbf{k})$ either of $\mathbb{Q}^{(k)}_{l\xi}(\mathbf{k})$, $\mathbb{T}^{(k)}_{l\xi}(\mathbf{k})$ or unity. Then $\{\mathbb{F}_{l\xi}(\mathbf{k})\}$ constitutes the orthonormalized complete set, i.e.,

$$\frac{1}{N_0} \sum_{\mathbf{k}} \mathbb{F}^{*}_{l_1\xi_1}(\mathbf{k})\mathbb{F}'_{l_2\xi_2}(\mathbf{k}) = \delta_{l_1,l_2}\delta_{\xi_1,\xi_2}\delta_{F,F'}, \tag{23}$$

$$\sum_{Fl\xi} \mathbb{F}_{l\xi}(\mathbf{k})\mathbb{F}^{*}_{l\xi}(\mathbf{k}') = \delta_{\mathbf{k},\mathbf{k}'}, \tag{24}$$

where N_0 is the number of $\mathbf{k}$ points, and the summation is taken over the minimal periodic unit in which

$$\frac{1}{N_0} \sum_{\mathbf{k}} \cos(\mathbf{k} \cdot \mathbf{b}_i)\cos(\mathbf{k} \cdot \mathbf{b}_j) = \frac{1}{2}\delta_{ij},$$

$$\frac{1}{N_0} \sum_{\mathbf{k}} \sin(\mathbf{k} \cdot \mathbf{b}_i)\sin(\mathbf{k} \cdot \mathbf{b}_j) = \frac{1}{2}\delta_{ij},$$

$$\frac{1}{N_0} \sum_{\mathbf{k}} \cos(\mathbf{k} \cdot \mathbf{b}_i)\sin(\mathbf{k} \cdot \mathbf{b}_j) = 0. \tag{25}$$

FIG. 3. (a) Full matrix form of SAMB $\hat{\mathbb{Z}}_{l\xi,sk}$, (b) atomic SAMB $\mathbb{X}_{l_1\xi_1,sk}$ with respect to atomic orbitals in each site or bond, and (c) cluster SAMB $\mathbb{Y}_{l_2\xi_2}$ for each site/bond clusters.

TABLE VIII. Notations used in this paper. SAMB and CG are the abbreviations of Symmetry-Adapted Multipole Basis and Clebsch-Gordan, respectively.

Symbol	Meaning
Q, G, M, T	electric (E), electric-toroidal (ET), magnetic (M), and magnetic-toroidal (MT) multipoles
l, m	rank $(0, 1, 2, \cdots)$ and component $(-l, -l+1, \cdots, l)$
$\xi = (\Gamma, n, \gamma)$	irrep., multiplicity, and component in point group
s, k	charge $(s = 0, k = 0)$ sector or spin $(s = 1, k = -1, 0, 1)$ sector for atomic SAMB
$O_{lm}(\boldsymbol{r})$	normalized spherical harmonics, $\boldsymbol{r} = (x, y, z)$
$O_{l\xi}(\boldsymbol{r})$	symmetry-adapted harmonics in point group
$U^{(l)}_{m,\xi}$	unitary matrix from (l, m) to (l, ξ) basis
$\overline{\mathbb{Q}}_{l\xi}$	SAMB for virtual cluster
$\mathbb{Q}^{(a)}_{l\xi,sk}, \mathbb{G}^{(a)}_{l\xi,sk}, \mathbb{M}^{(a)}_{l\xi,sk}, \mathbb{T}^{(a)}_{l\xi,sk}$	SAMB for atomic degrees of freedom
$\mathbb{Q}^{(s)}_{l\xi}$	SAMB for site cluster
$\mathbb{Q}^{(b)}_{l\xi}, \mathbb{T}^{(b)}_{l\xi}$	SAMB for bond cluster (symmetric part, antisymmetric part)
$\mathbb{Q}^{(u)}_{l\xi}, \mathbb{T}^{(u)}_{l\xi}$	uniform component of $\mathbb{Q}^{(b)}_{l\xi}(\boldsymbol{k}), \mathbb{T}^{(b)}_{l\xi}(\boldsymbol{k})$ having off-diagonal matrix elements only
$\mathbb{Q}^{(k)}_{l\xi}(\boldsymbol{k}), \mathbb{T}^{(k)}_{l\xi}(\boldsymbol{k})$	structure factor obtained from $\mathbb{Q}^{(b)}_{l\xi}, \mathbb{T}^{(b)}_{l\xi}$
$\hat{\mathbb{Q}}_{l\xi,sk}, \hat{\mathbb{G}}_{l\xi,sk}, \hat{\mathbb{M}}_{l\xi,sk}, \hat{\mathbb{T}}_{l\xi,sk}$	combined SAMB (isolated cluster systems)
$\hat{\mathbb{Q}}_{l\xi,sk}(\boldsymbol{k}), \hat{\mathbb{G}}_{l\xi,sk}(\boldsymbol{k}), \hat{\mathbb{M}}_{l\xi,sk}(\boldsymbol{k}), \hat{\mathbb{T}}_{l\xi,sk}(\boldsymbol{k})$	combined SAMB (periodic crystals)
$\mathbb{X}_{l\xi,sk}$	SAMB for $\{ \mathbb{Q}^{(a)}_{l\xi,sk}, \mathbb{G}^{(a)}_{l\xi,sk}, \mathbb{M}^{(a)}_{l\xi,sk}, \mathbb{T}^{(a)}_{l\xi,sk} \}$
$\mathbb{Y}_{l\xi}$	SAMB for $\{ \mathbb{Q}^{(s)}_{l\xi}, \mathbb{Q}^{(b)}_{l\xi}, \mathbb{T}^{(b)}_{l\xi} \}$
$\hat{\mathbb{Z}}_{l\xi,sk}$	combined SAMB for $\mathbb{X}_{l_1\xi_1,sk}$ and $\mathbb{Y}_{l_2\xi_2}$
$\mathbb{U}_{l\xi}$	SAMB for $\{ \mathbb{Q}^{(s)}_{l\xi}, \mathbb{Q}^{(u)}_{l\xi}, \mathbb{T}^{(u)}_{l\xi} \}$ (isolated cluster systems/periodic crystals)
$\mathbb{F}_{l\xi}(\boldsymbol{k})$	SAMB for $\{ \mathbb{Q}^{(k)}_{l\xi}(\boldsymbol{k}), \mathbb{T}^{(k)}_{l\xi}(\boldsymbol{k}), 1 \}$ (periodic crystals)
$C^{l_1\xi_1,l_2\xi_2}_{l\xi}(X, Y|Z)$	CG coefficient from $\mathbb{X}_{l_1\xi_1,sk}$ and $\mathbb{Y}_{l_2\xi_2}$ to $\mathbb{Z}_{l\xi,sk}$ (isolated cluster systems/periodic crystals)
$C^{l_1\xi_1,l_2\xi_2,l_3\xi_3}_{l\xi}(X, U, F|Z)$	CG coefficient from $\mathbb{X}_{l_1\xi_1,sk}$, $\mathbb{U}_{l_2\xi_2}$, and $\mathbb{F}_{l_3\xi_3}(\boldsymbol{k})$ to $\mathbb{Z}_{l\xi,sk}(\boldsymbol{k})$ (periodic crystals)

It should be noted that the periodicity of $\mathbb{F}_{l\xi}(\boldsymbol{k})$ differs from the Brillouin zone of the system, unless the bond vectors are identical to the lattice vector in the primitive unit cell.

By using $\mathbb{F}_{l\xi}(\boldsymbol{k})$, we can reexpress $\mathbb{Y}_{l\xi}(\boldsymbol{k})$ as

$$\mathbb{Y}_{l\xi}(\boldsymbol{k}) = \sum_{l_1\xi_1 l_2\xi_2} f^{l_1\xi_1,l_2\xi_2}_{l\xi}(U, F) \, \mathbb{U}_{l_1\xi_1} \otimes \mathbb{F}_{l_2\xi_2}(\boldsymbol{k}), \quad (26)$$

where $\mathbb{U}_{l\xi} = \mathbb{Q}^{(s)}_{l\xi}$ for site clusters or the uniform component $\mathbb{Y}_{l\xi}(\boldsymbol{k} = 0)$ having only off-diagonal matrix elements for bond clusters, with appropriate normalization. Here $f^{l_1\xi_1,l_2\xi_2}_{l\xi}(U, F)$ is the linear coefficient. Note that $\mathbb{U}_{l\xi} = \mathbb{Y}_{l\xi}$ for isolated cluster systems.

By these prescriptions, we finally obtain the combined SAMB in terms of the uniform and structure SAMBs as

$$\hat{\mathbb{Z}}_{l\xi,sk}(\boldsymbol{k}) = \sum_{\xi_1, l_3\xi_3 l_4\xi_4} C^{l_1\xi_1,l_3\xi_3,l_4\xi_4}_{l\xi}(X, U, F|Z)$$

$$\times \mathbb{X}_{l_1\xi_1,sk} \otimes \mathbb{U}_{l_3\xi_3} \otimes \mathbb{F}_{l_4\xi_4}(\boldsymbol{k}), \quad (27)$$

where

$$C^{l_1\xi_1,l_3\xi_3,l_4\xi_4}_{l\xi}(X, U, F|Z)$$

$$\equiv \sum_{\xi_2} C^{l_1\xi_1,l_2\xi_2}_{l\xi}(X, Y|Z) f^{l_3\xi_3,l_4\xi_4}_{l_2\xi_2}(U, F). \quad (28)$$

The notations and their meanings used in this paper are summarized in Table VIII.

III. APPLICATION TO GRAPHENE

In this section, we demonstrate the symmetry-adapted TB modeling for graphene based on our method. Then, using the obtained TB model, we determine the model parameters by optimizing them to reproduce the energy dispersion obtained by the DF computation.

A. TB model based on SAMB

Graphene has a honeycomb structure in space group $P6/mmm$ (#191, D^1_{6h}). The lattice constant is $a = 2.435$ Å, the length of the vacuum layer along the c axis is set as $c = 4a$, and the unit vectors are given by $\boldsymbol{a}_1 = (1, 0, 0)a$, $\boldsymbol{a}_2 = (-1/2, \sqrt{3}/2, 0)a$, and $\boldsymbol{a}_3 = (0, 0, 1)c$. The symmetry operations of D_{6h} point group are given in Table IX.

There are two C atoms in the unit cell, and we consider the spinless p_z orbital at each C atom and up to sixth-neighbor bonds. The site cluster C, the bond clusters B_1, and B_2 for three nearest-neighbor and six second-neighbor bonds are summarized in Table X and Fig. 4. In constructing the virtual cluster sites in D_{6h}, we have used the general point, $\boldsymbol{r}_1 = (\sqrt{3} + 1, \sqrt{3} - 1, 1)$ and its symmetry-operated points. By the mapping procedure from the virtual cluster as explained in Sec. II A 3, we obtain the SAMB for the site/bond clusters in Table XI. The SAMBs for the clusters C and B_1 are schematically shown in Fig. 5.

TABLE IX. Symmetry operations (SOs) in D_{6h}.

No.	SO	No.	SO	No.	SO	No.	SO
1	1	2	2_{001}	3	2_{100}	4	2_{010}
5	2_{110}	6	2_{120}	7	2_{210}	8	2_{1-10}
9	3_{001}^+	10	3_{001}^-	11	6_{001}^+	12	6_{001}^-
13	-1	14	m_{100}	15	m_{010}	16	m_{110}
17	m_{001}	18	m_{120}	19	m_{210}	20	m_{1-10}
21	-3_{001}^+	22	-3_{001}^-	23	-6_{001}^+	24	-6_{001}^-

In this example, since there is only one atomic SAMB for spinless p_z bra-ket space,

$$\mathbb{Q}_{0,A_{1g},(0,0)}^{(a)} = (1), \tag{29}$$

the combined SAMB is always equivalent to $\mathbb{Y}_{l\xi}(\boldsymbol{k})$, i.e., $\hat{\mathbb{Z}}_{l\xi}(\boldsymbol{k}) = \mathbb{Y}_{l\xi}(\boldsymbol{k})$. Thus, we omit $\mathbb{Q}_{0,A_{1g},(0,0)}^{(a)}$ hereafter. Converting $\mathbb{Y}_{l\xi}$ to the momentum-space representation in 2×2 full matrix form ($|p_z@C_1\rangle$, $|p_z@C_2\rangle$), we obtain $\mathbb{Y}_{l\xi}(\boldsymbol{k}) = \hat{\mathbb{Z}}_{l\xi}(\boldsymbol{k})$ for the site cluster C and the nearest-neighbor bond cluster B_1 as

$$\hat{\mathbb{Q}}_{0,A_{1g}}^{[C]} = \frac{1}{\sqrt{2}}\begin{pmatrix} 1 & 0 \\ 0 & 1 \end{pmatrix}, \quad \hat{\mathbb{Q}}_{3,B_{1u}}^{[C]} = \frac{1}{\sqrt{2}}\begin{pmatrix} 1 & 0 \\ 0 & -1 \end{pmatrix}, \tag{30}$$

$$\hat{\mathbb{Q}}_{0,A_{1g}}^{[B_1]}(\boldsymbol{k}) = \frac{1}{\sqrt{6}}\begin{pmatrix} 0 & e^{-i\boldsymbol{k}\cdot\boldsymbol{b}_1} + e^{-i\boldsymbol{k}\cdot\boldsymbol{b}_2} + e^{-i\boldsymbol{k}\cdot\boldsymbol{b}_3} \\ \text{c.c.} & 0 \end{pmatrix},$$

$$\hat{\mathbb{Q}}_{2,E_{2g},u}^{[B_1]}(\boldsymbol{k}) = \frac{1}{2\sqrt{3}}\begin{pmatrix} 0 & 2e^{-i\boldsymbol{k}\cdot\boldsymbol{b}_1} - e^{-i\boldsymbol{k}\cdot\boldsymbol{b}_2} - e^{-i\boldsymbol{k}\cdot\boldsymbol{b}_3} \\ \text{c.c.} & 0 \end{pmatrix},$$

$$\hat{\mathbb{Q}}_{2,E_{2g},v}^{[B_1]}(\boldsymbol{k}) = \frac{1}{2}\begin{pmatrix} 0 & -e^{-i\boldsymbol{k}\cdot\boldsymbol{b}_2} + e^{-i\boldsymbol{k}\cdot\boldsymbol{b}_3} \\ \text{c.c.} & 0 \end{pmatrix}, \tag{31}$$

TABLE X. C-site cluster (C) and the nearest-neighbor (B_1) and second-neighbor (B_2) bond clusters in graphene and the one-to-many correspondences $g(i)$.

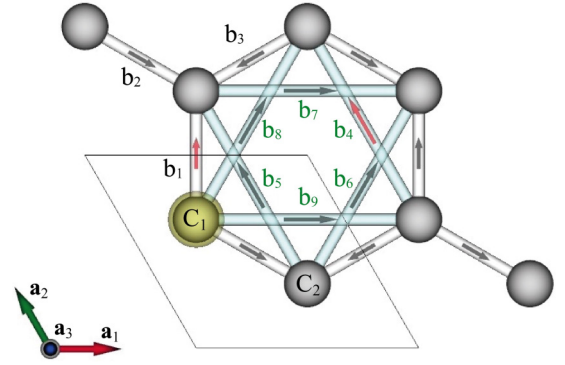| C	$\boldsymbol{R}_i$	$g(i)$
C_1	$[\frac{1}{3}, \frac{2}{3}, 0]$	$[1,6,7,8,9,10,14,15,16,17,23,24]$
C_2	$[\frac{2}{3}, \frac{1}{3}, 0]$	$[2,3,4,5,11,12,13,18,19,20,21,22]$
B_1	$\boldsymbol{b}_i@\boldsymbol{c}_i$	$g(i)$
b_1	$[\frac{1}{3}, \frac{2}{3}, 0]@[\frac{1}{2}, 0, 0]$	$[1,-2,-3,6,-13,14,17,-18]$
b_2	$[\frac{1}{3}, -\frac{1}{3}, 0]@[\frac{1}{2}, \frac{1}{2}, 0]$	$[-4,7,10,-11,15,-19,-22,23]$
b_3	$[-\frac{2}{3}, -\frac{1}{3}, 0]@[0, \frac{1}{2}, 0]$	$[-5,8,9,-12,16,-20,-21,24]$
B_2	$\boldsymbol{b}_i@\boldsymbol{c}_i$	$g(i)$
b_4	$[0, 1, 0]@[\frac{1}{3}, \frac{1}{6}, 0]$	$[1,-7,-15,17]$
b_5	$[0, 1, 0]@[\frac{2}{3}, \frac{5}{6}, 0]$	$[-2,4,-13,19]$
b_6	$[1, 1, 0]@[\frac{1}{6}, \frac{5}{6}, 0]$	$[-3,12,-18,21]$
b_7	$[1, 0, 0]@[\frac{1}{6}, \frac{1}{6}, 0]$	$[5,-11,20,-22]$
b_8	$[1, 1, 0]@[\frac{5}{6}, \frac{1}{6}, 0]$	$[6,-9,14,-24]$
b_9	$[1, 0, 0]@[\frac{5}{6}, \frac{2}{3}, 0]$	$[-8,10,-16,23]$

FIG. 4. Site cluster and nearest-neighbor and second-neighbor bond clusters in graphene. The representative site and bonds are indicated by the yellow circle and red arrows, respectively.

$$\hat{\mathbb{T}}_{1,E_{1u},u}^{[B_1]}(\boldsymbol{k}) = \frac{1}{2}\begin{pmatrix} 0 & ie^{-i\boldsymbol{k}\cdot\boldsymbol{b}_2} - ie^{i\boldsymbol{k}\cdot\boldsymbol{b}_3} \\ \text{c.c.} & 0 \end{pmatrix},$$

$$\hat{\mathbb{T}}_{1,E_{1u},v}^{[B_1]}(\boldsymbol{k}) = \frac{1}{2\sqrt{3}}\begin{pmatrix} 0 & 2ie^{-i\boldsymbol{k}\cdot\boldsymbol{b}_1} - ie^{-i\boldsymbol{k}\cdot\boldsymbol{b}_2} - ie^{-i\boldsymbol{k}\cdot\boldsymbol{b}_3} \\ \text{c.c.} & 0 \end{pmatrix},$$

$$\hat{\mathbb{T}}_{3,B_{1u}}^{[B_1]}(\boldsymbol{k}) = \frac{1}{\sqrt{6}}\begin{pmatrix} 0 & ie^{-i\boldsymbol{k}\cdot\boldsymbol{b}_1} + ie^{-i\boldsymbol{k}\cdot\boldsymbol{b}_2} + ie^{-i\boldsymbol{k}\cdot\boldsymbol{b}_3} \\ \text{c.c.} & 0 \end{pmatrix}, \tag{32}$$

where "c.c." denotes the complex conjugate of the corresponding element in the upper-triangle of the matrix and square brackets in the superscript indicate the relevant site/bond clusters. We have omitted the superscripts, (s) and (b), as we have attached the cluster indices. In the same procedure, the full matrix forms in the momentum representation for more than second-neighbor bond clusters, B_2, B_3, . . . , may be obtained.

By selecting the identity representation A_{1g}, e.g., $\hat{\mathbb{Q}}_{0,A_{1g}}^{[C]}$ and $\hat{\mathbb{Q}}_{0,A_{1g}}^{[B_1]}(\boldsymbol{k})$, we obtain the TB Hamiltonian in terms of the
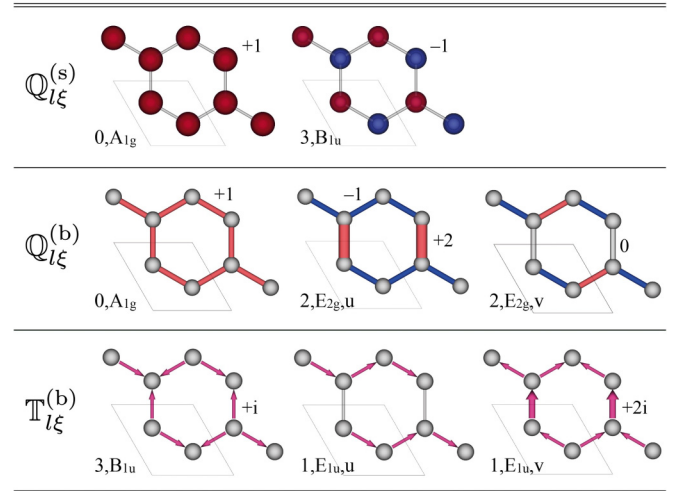

FIG. 5. Site cluster and the nearest-neighbor bond cluster SAMBs for graphene. The color and size (width) represent the weight of the components in each SAMB.

TABLE XI. SAMB in C site cluster and B₁ and B₂ bond clusters.

l	Γ	n	γ	$\mathbb{Q}_{l\xi}^{(s)}$ for C	l	Γ	n	γ	$\mathbb{Q}_{l\xi}^{(s)}$ for C
0	A_{1g}	–	–	$\frac{1}{\sqrt{2}}(1,1)$	3	B_{1u}	–	–	$\frac{1}{\sqrt{2}}(1,-1)$

l	Γ	n	γ	$\mathbb{Q}_{l\xi}^{(b)}$ for B₁	l	Γ	n	γ	$\mathbb{T}_{l\xi}^{(b)}$ for B₁
0	A_{1g}	–	–	$\frac{1}{\sqrt{3}}(1,1,1)$	1	E_{1u}	–	u	$\frac{i}{\sqrt{2}}(0,1,-1)$
2	E_{2g}	–	u	$\frac{1}{\sqrt{6}}(2,-1,-1)$			–	v	$\frac{i}{\sqrt{6}}(2,-1,-1)$
			v	$\frac{1}{\sqrt{2}}(0,-1,1)$	3	B_{1u}	–	–	$\frac{i}{\sqrt{3}}(1,1,1)$

l	Γ	n	γ	$\mathbb{Q}_{l\xi}^{(b)}$ for B₂
0	A_{1g}	–	–	$\frac{1}{\sqrt{6}}(1,1,1,1,1,1)$
1	E_{1u}	–	u	$\frac{1}{2}(1,-1,1,0,-1,0)$
			v	$\frac{1}{2\sqrt{3}}(1,-1,-1,2,1,-2)$
2	E_{2g}	–	u	$\frac{1}{2\sqrt{3}}(1,1,1,-2,1,-2)$
			v	$\frac{1}{2}(-1,-1,1,0,1,0)$
3	B_{1u}	–	–	$\frac{1}{\sqrt{6}}(1,-1,-1,-1,1,1)$

l	Γ	n	γ	$\mathbb{T}_{l\xi}^{(b)}$ for B₂
1	E_{1u}	–	u	$\frac{i}{2\sqrt{3}}(1,1,-1,-2,-1,-2)$
			v	$-\frac{i}{2}(1,1,1,0,1,0)$
2	E_{2g}	–	u	$\frac{i}{2}(1,-1,-1,0,1,0)$
			v	$\frac{i}{2\sqrt{6}}(1,-1,1,2,-1,-2)$
3	B_{2u}	–	–	$\frac{i}{\sqrt{6}}(1,1,-1,1,-1,1)$
6	A_{2g}	–	–	$\frac{i}{\sqrt{6}}(1,-1,1,-1,-1,1)$

combined SAMBs as

$$H(\boldsymbol{k}) = \sum_j z_j \hat{\mathbb{Z}}_j(\boldsymbol{k})$$
$$= z_1 \hat{\mathbb{Q}}_0^{[C]} + z_2 \hat{\mathbb{Q}}_0^{[B_1]}(\boldsymbol{k}) + z_3 \hat{\mathbb{Q}}_0^{[B_2]}(\boldsymbol{k}) + \cdots, \quad (33)$$

where the irrep. A_{1g} has been omitted. Here $j = 1, 2, \ldots,$ is the sequential number for the combined SAMBs, and the coefficient z_j is the weight of each SAMB. They will be determined by comparing the energy dispersion obtained from the TB model with that of the DF computation.

$\mathbb{Y}_{l\xi}(\boldsymbol{k}) = \hat{\mathbb{Z}}_{l\xi}(\boldsymbol{k})$ can be further decomposed into the direct product of $\mathbb{U}_{l\xi}$ and $\mathbb{F}_{l\xi}(\boldsymbol{k})$. In addition to the diagonal $\mathbb{Q}_{l\xi}^{(s)}$ from the site cluster C, the uniform matrices $\mathbb{Q}_{l\xi}^{(u)}$ and $\mathbb{T}_{l\xi}^{(u)}$ are obtained by the off-diagonal $\mathbb{Q}_{l\xi}^{(b)}(\boldsymbol{k})$ and $\mathbb{T}_{l\xi}^{(b)}(\boldsymbol{k})$ with $\boldsymbol{k} = 0$ and appropriate normalization as

$$\mathbb{Q}_{0,A_{1g}}^{[B_1]} = \frac{1}{\sqrt{2}}\begin{pmatrix} 0 & 1 \\ 1 & 0 \end{pmatrix}, \quad \mathbb{T}_{3,B_{1u}}^{[B_1]} = \frac{1}{\sqrt{2}}\begin{pmatrix} 0 & i \\ -i & 0 \end{pmatrix}. \quad (34)$$

Note that since Eqs. (30) and (34) form the complete set for 2×2 space, the uniform matrices $\mathbb{Q}_{l\xi}^{[B_1]}$ and $\mathbb{T}_{l\xi}^{[B_1]}$ are common for all bond clusters.

By Eq. (22), the structure SAMBs are given by

$$\mathbb{Q}_{0,A_{1g}}^{[B_1](k)}(\boldsymbol{k}) = \frac{2}{\sqrt{6}}(c_1 + c_2 + c_3),$$

$$\mathbb{Q}_{2,E_{2g},u}^{[B_1](k)}(\boldsymbol{k}) = \frac{1}{\sqrt{3}}(2c_1 - c_2 - c_3),$$

$$\mathbb{Q}_{2,E_{2g},v}^{[B_1](k)}(\boldsymbol{k}) = -c_2 + c_3,$$

$$\mathbb{T}_{1,E_{1u},u}^{[B_1](k)}(\boldsymbol{k}) = s_2 - s_3,$$

$$\mathbb{T}_{1,E_{1u},v}^{[B_1](k)}(\boldsymbol{k}) = \frac{1}{\sqrt{3}}(2s_1 - s_2 - s_3),$$

$$\mathbb{T}_{3,B_{1u}}^{[B_1](k)}(\boldsymbol{k}) = \frac{2}{\sqrt{6}}(s_1 + s_2 + s_3), \quad (35)$$

where $c_i = \cos(\boldsymbol{k} \cdot \boldsymbol{b}_i)$ and $s_i = \sin(\boldsymbol{k} \cdot \boldsymbol{b}_i)$ with the reduced momentum $\boldsymbol{k} = 2\pi(k_1, k_2, k_3)$. The expressions can be converted in terms of the Cartesian coordinate k_x and k_y by substituting $k_1 = k_x a$ and $k_2 = (-k_x a + \sqrt{3}k_y a)/2$. The $\boldsymbol{k}$ dependence of $\mathbb{Q}_{0,A_{1g}}^{[B_1](k)}(\boldsymbol{k})$ and $\mathbb{T}_{3,B_{1u}}^{[B_1](k)}(\boldsymbol{k})$ are shown in Fig. 6.
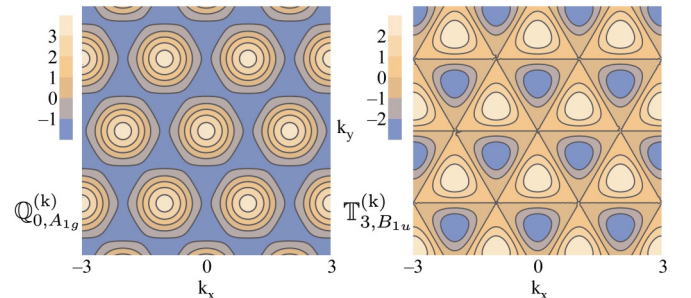

FIG. 6. Symmetry-adapted structure factors for the nearest-neighbor bonds in graphene. k_x and k_y are in unit of $2\pi/a$.

TABLE XII. Bond vectors for graphene up to sixth neighbors.

n	$\boldsymbol{b}_i$	Vector	$\boldsymbol{b}_i$	Vector	$\boldsymbol{b}_i$	Vector
1	$\boldsymbol{b}_1$	$[\frac{1}{3}, \frac{2}{3}, 0]$	$\boldsymbol{b}_2$	$[\frac{1}{3}, -\frac{1}{3}, 0]$	$\boldsymbol{b}_3$	$[-\frac{2}{3}, -\frac{1}{3}, 0]$
2	$\boldsymbol{b}_4$	$[0, 1, 0]$	$\boldsymbol{b}_5$	$= \boldsymbol{b}_4$	$\boldsymbol{b}_6$	$[1, 1, 0]$
	$\boldsymbol{b}_7$	$[1, 0, 0]$	$\boldsymbol{b}_8$	$= \boldsymbol{b}_6$	$\boldsymbol{b}_9$	$= \boldsymbol{b}_7$
3	$\boldsymbol{b}_{10}$	$[\frac{4}{3}, \frac{2}{3}, 0]$	$\boldsymbol{b}_{11}$	$[-\frac{2}{3}, \frac{2}{3}, 0]$	$\boldsymbol{b}_{12}$	$[-\frac{2}{3}, -\frac{4}{3}, 0]$
4	$\boldsymbol{b}_{13}$	$[\frac{4}{3}, \frac{5}{3}, 0]$	$\boldsymbol{b}_{14}$	$[\frac{1}{3}, \frac{5}{3}, 0]$	$\boldsymbol{b}_{15}$	$[\frac{4}{3}, -\frac{1}{3}, 0]$
	$\boldsymbol{b}_{16}$	$[-\frac{5}{3}, -\frac{4}{3}, 0]$	$\boldsymbol{b}_{17}$	$[-\frac{5}{3}, -\frac{1}{3}, 0]$	$\boldsymbol{b}_{18}$	$[\frac{1}{3}, -\frac{4}{3}, 0]$
5	$\boldsymbol{b}_{19}$	$[1, 2, 0]$	$\boldsymbol{b}_{20}$	$= -\boldsymbol{b}_{19}$	$\boldsymbol{b}_{21}$	$[-1, 1, 0]$
	$\boldsymbol{b}_{22}$	$[2, 1, 0]$	$\boldsymbol{b}_{23}$	$= -\boldsymbol{b}_{21}$	$\boldsymbol{b}_{24}$	$= -\boldsymbol{b}_{22}$
6	$\boldsymbol{b}_{25}$	$[2, 2, 0]$	$\boldsymbol{b}_{26}$	$= \boldsymbol{b}_{25}$	$\boldsymbol{b}_{27}$	$[0, 2, 0]$
	$\boldsymbol{b}_{28}$	$[2, 0, 0]$	$\boldsymbol{b}_{29}$	$= \boldsymbol{b}_{27}$	$\boldsymbol{b}_{30}$	$= \boldsymbol{b}_{28}$

Using $\mathbb{U}_{l\xi}$ and $\mathbb{F}_{l\xi}(\boldsymbol{k})$, $\hat{\mathbb{Q}}_0^{[B_n]}(\boldsymbol{k})$ for $n = 1, 3, 4$ can be decomposed as

$$\hat{\mathbb{Q}}_0^{[B_n]}(\boldsymbol{k}) = \frac{1}{\sqrt{2}} \left[\mathbb{Q}_{0,A_{1g}}^{[B_1]} \otimes \mathbb{Q}_{0,A_{1g}}^{[B_n](k)}(\boldsymbol{k}) - \mathbb{T}_{3,B_{1u}}^{[B_1]} \otimes \mathbb{T}_{3,B_{1u}}^{[B_n](k)}(\boldsymbol{k}) \right],$$

(36)

and for $n = 2, 5, 6$ as

$$\hat{\mathbb{Q}}_0^{[B_n]}(\boldsymbol{k}) = \mathbb{Q}_{0,A_{1g}}^{[C]} \otimes \mathbb{Q}_{0,A_{1g}}^{[B_n](k)}(\boldsymbol{k}).$$

(37)

Here the structure factors for $n = 3, 4$ are given by

$$\mathbb{Q}_{0,A_{1g}}^{[B_3](k)}(\boldsymbol{k}) = \frac{2}{\sqrt{6}}(c_{10} + c_{11} + c_{12}),$$

$$\mathbb{Q}_{0,A_{1g}}^{[B_4](k)}(\boldsymbol{k}) = \frac{1}{\sqrt{3}}(c_{13} + c_{14} + c_{15} + c_{16} + c_{17} + c_{18}),$$

$$\mathbb{T}_{3,B_{1u}}^{[B_3](k)}(\boldsymbol{k}) = \frac{2}{\sqrt{6}}(s_{10} + s_{11} + s_{12}),$$

$$\mathbb{T}_{3,B_{1u}}^{[B_4](k)}(\boldsymbol{k}) = \frac{1}{\sqrt{3}}(s_{13} + s_{14} + s_{15} + s_{16} + s_{17} + s_{18}), \quad (38)$$

and for $n = 2, 5, 6$,

$$\mathbb{Q}_{0,A_{1g}}^{[B_2](k)}(\boldsymbol{k}) = \frac{2}{\sqrt{6}}(c_4 + c_6 + c_7),$$

$$\mathbb{Q}_{0,A_{1g}}^{[B_5](k)}(\boldsymbol{k}) = \frac{2}{\sqrt{6}}(c_{19} + c_{21} + c_{22}),$$

$$\mathbb{Q}_{0,A_{1g}}^{[B_6](k)}(\boldsymbol{k}) = \frac{2}{\sqrt{6}}(c_{25} + c_{27} + c_{28}),$$

(39)

where the bond vectors up to sixth neighbors are shown in Table XII.

By using the SAMB, the symmetry-breaking terms are classified according to point-group symmetry, which is useful to narrow down the possible order parameters in the phase transition. For example, the mass term which lowers the symmetry from D_{6h} to D_{3h} is given by $\hat{\mathbb{Q}}_{3,B_{1u}}^{[C]}$. In the ordered phase, this term becomes the identity irrep.

Similarly, the Haldane's magnetic flux due to kinetic spin-orbit coupling is expressed as $\hat{\mathbb{M}}_{1,A_{2g}}^{[B_2]} = \mathbb{Q}_{3,B_{1u}}^{[C]} \otimes \mathbb{T}_{3,B_{2u}}^{[B_2](k)}$ where the structure factor is $\mathbb{T}_{3,B_{2u}}^{[B_2](k)} = \frac{2}{\sqrt{6}}(s_5 - s_6 + s_7)$,

which corresponds to the vortexlike imaginary hopping in second-neighbor A-A or B-B bonds (see Fig. 4) [24].

When the inversion symmetry is broken, e.g., by applying an electric field perpendicular to the plane, the Rashba term appears [25]. As the polar vector belongs to A_{2u} irrep., we look for the SAMB belonging to A_{2u}. Although there is no SAMB belonging to A_{2u} in the spinless Hilbert space, it can appear when taking into account the spin degree of freedom ($\sigma_x, \sigma_y, \sigma_z$). Considering the product decomposition, $A_{2u} = A_{2g} \otimes A_{1u}$ or $A_{2u} = E_{1g} \otimes E_{1u}$ and the irrep. of the spins as σ_z (A_{2g}) and ($-\sigma_y, \sigma_x$) (E_{1g}), we obtain the Rashba term for the nearest-neighbor bond cluster as

$$H_{\text{Rashba}}(\boldsymbol{k}) = \frac{1}{2} \left[-\sigma_y \otimes \mathbb{Q}_{0,A_{1g}}^{[B_1]} \otimes \mathbb{T}_{1,E_{1u},u}^{[B_1](k)}(\boldsymbol{k}) \right.$$
$$\left. + \sigma_x \otimes \mathbb{Q}_{0,A_{1g}}^{[B_1]} \otimes \mathbb{T}_{1,E_{1u},v}^{[B_1](k)}(\boldsymbol{k}) \right]. \quad (40)$$

In this way, the symmetry-breaking terms are easily classified in terms of the SAMB, and their $\boldsymbol{k}$ dependence is encoded in the structure SAMB, $\mathbb{F}_{l\xi}(\boldsymbol{k})$.

For obtaining deeper insights into the physical responses and the exploration of more efficient materials, it is highly desirable to achieve a microscopic understanding of the relevant mechanism and the essential parameters. In this sense, the symmetry-adapted modeling as Eq. (33) is also useful to analyze various linear and nonlinear response functions, which bridges the gap between the phenomenological approaches and DF computations [14,26]. The systematic analysis method for response functions proposed in Refs. [14,27] not only enables one to predict the possible responses but also extract essential parameters in a systematic manner by analyzing the indicators such as

$$\Gamma_{\mu;\alpha}^{ij} = \text{Tr}[A_\mu H^i B_\alpha H^j],$$
$$\Gamma_{\mu;\alpha,\beta}^{ijk} = \text{Tr}[A_\mu H^i B_\alpha H^j B_\beta H^k], \quad (41)$$

for linear and second-order nonlinear responses. The corresponding response becomes active when the indicator is nonzero. Here A and B are the output and input operators in the responses, respectively, and H^i is the ith power of the Hamiltonian matrices. By using Eq. (33), the trace in the indicator is regarded as selecting the identity irrep. in the irreducible decomposition of the product of A, B, and H^i. Thus, the combination of those operators giving the identity irrep. is nothing but the essential parameters of the response. It can provide us with guidelines for future material design, beyond those obtained by the existing phenomenological approaches and DF calculations.

B. Optimization of TB Model

We have constructed the TB model for graphene in Eq. (33), and there are seven parameters $z = (z_1, z_2, \ldots, z_7)$ up to sixth-neighbor hoppings. In order to optimize the model parameters z, we compute the energy dispersion by DF computation.

For the DF computation, we have used the Quantum ESPRESSO open-software package [28] with the Perdew-Zunger correlation functional [29] and the ultrasoft pseudopotential. We have used the $\boldsymbol{k}$ grid, $(N_1, N_2, N_3) = (12, 12, 1)$, and the kinetic energy cutoff of the Kohn-Sham wave
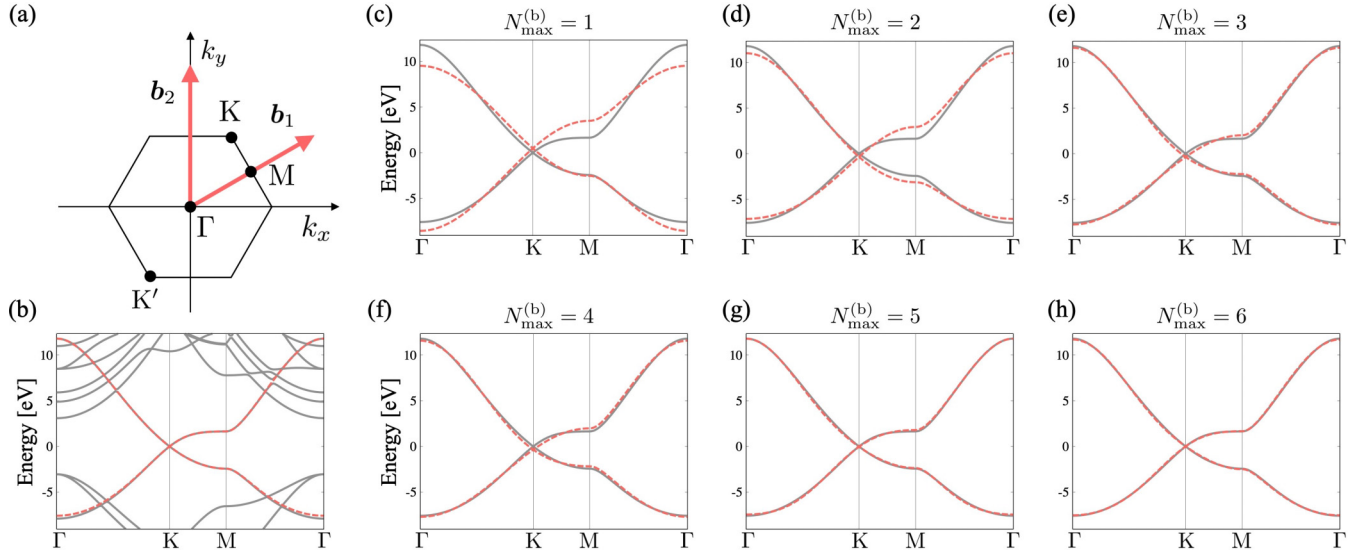
FIG. 7. The comparisons of the band dispersion between the DF Wannier and SAMB TB models. (a) The Brillouin zone and high-symmetry points, (b) the comparison of energy dispersions between DF (gray solid lines) and Wanner TB model (red dashed lines), and [(c)–(h)] the comparison of energy dispersion between the DF Wannier TB model (gray solid lines) and our SAMB TB model up to $N_{\mathrm{max}}^{(\mathrm{b})}$-neighbor bonds (red dashed lines). The Fermi energy is set as the origin.

functions and convergence threshold are set as 30 Ry and 1×10^{-10} Ry, respectively.

The obtained electronic bands near the Fermi energy in the high-symmetry lines Γ-K-M-Γ in Fig. 7(a) are entangled as shown in Fig. 7(b) (gray solid lines). Thus, before optimizing the model parameters, two relevant bands near the Fermi energy must be disentangled. For this purpose, we have used the Wannier90 open-source software package [7–9]: The p_z orbital is chosen for each C atom as the initial guess function, and the outer and inner energy windows are set as [−30, 12] eV and [−3.0, 2.6] eV, respectively. Then, we obtain the p_z-like two Wannier orbitals and corresponding energy dispersions are indicated by red dashed lines as shown in Fig. 7(b).

In the optimization process, we introduce the loss function as the dimensionless mean-squared error of the normalized energy eigenvalues between the DF and our TB models [26],

$$L(z) = \frac{1}{N_k N_n} \sum_n \sum_{\mathbf{k}} \left[\frac{\epsilon_{n\mathbf{k}}(z) - \epsilon_{n\mathbf{k}}^{\mathrm{DF}}}{W} \right]^2, \qquad (42)$$

where $N_k = 151$, $N_n = 2$, and $W = 21.40$ (eV) are the number of $\mathbf{k}$ points to evaluate the loss function, the size of the Hamiltonian, and band width, respectively.

In order to eliminate strong initial-guess dependence, we use the hidden layers in the neural network. Namely, the relation between the input DF energy bands $\epsilon_{n\mathbf{k}}^{\mathrm{DF}}$ and the resultant energy bands of our TB model $\epsilon_{n\mathbf{k}}(z)$ is regarded as the nontrivial nonlinear system. Then, we insert the hidden layers between the input and output energy bands to express flexibly this nonlinear relation and apply the back-propagation error algorithm to optimize the model parameters z and hyper parameters in the hidden layers [16,30]. It turned out that extremely low initial-guess dependence was achieved. We have chosen 50 $\mathbf{k}$ points in each line in the high-symmetry lines Γ-K-M-Γ and used $N_{\mathrm{h}} = 3$ hidden layers. We have used

the PyTorch package [31] and the Adam optimizer [32] with the learning rate $\alpha = 0.1$. The fixed maximum number of iterations $N_{\mathrm{iter}} = 250$ is sufficient to reach convergence. In the case of graphene, the construction of the SAMB and the optimization of the model parameters take within a minute by a standard laptop computer. For more complicated systems, the computing cost increases mostly in the part of the construction of the SAMB, but it takes within 10 minutes for SrVO$_3$ and MoS$_2$ as shown in the Supplemental Material.

The results of the best optimization with $N_{\mathrm{max}}^{(\mathrm{b})}$-neighbor bonds are shown in Figs. 7(c)–7(h), where the convergence value of the loss function for Fig. 7(h) is about 9.4×10^{-6}. With increase of $N_{\mathrm{max}}^{(\mathrm{b})}$, the result gives better reproduction of the DF energy dispersion. The optimization parameters for $N_{\mathrm{max}}^{(\mathrm{b})} = 6$ are obtained as

$$z_1 = -0.163, \quad z_2 = -7.274, \quad z_3 = 0.880, \quad z_4 = -0.693,$$
$$z_5 = 0.0761, \quad z_6 = 0.202, \quad z_7 = -0.080 \text{ (eV)}. \qquad (43)$$

The band structure, density of states (DOS), isoenergy surface, and bond-length dependence of the maximum strength of hoppings are obtained using these optimized parameters as shown in Fig. 8. The results of both models are in good agreement. On the other hand, as shown in Fig. 8(c), the bond length dependence of the maximum strength of hoppings differs significantly for the two models. In our SAMB TB model, the magnitude of the weight tends to decrease as the bond length increases, while that of the DF Wannier TB model shows long tail. The advantage of the SAMB TB is that the hopping range can be freely chosen without losing the symmetry of the system, and the systematic comparison with different hopping range is possible as shown in Figs. 7(c)–7(h).

The similar analysis has been performed for a chiral nonsymmorphic system of Te [26], a typical orbitally degenerate system of SrVO$_3$, and the spin-orbital coupled metal of
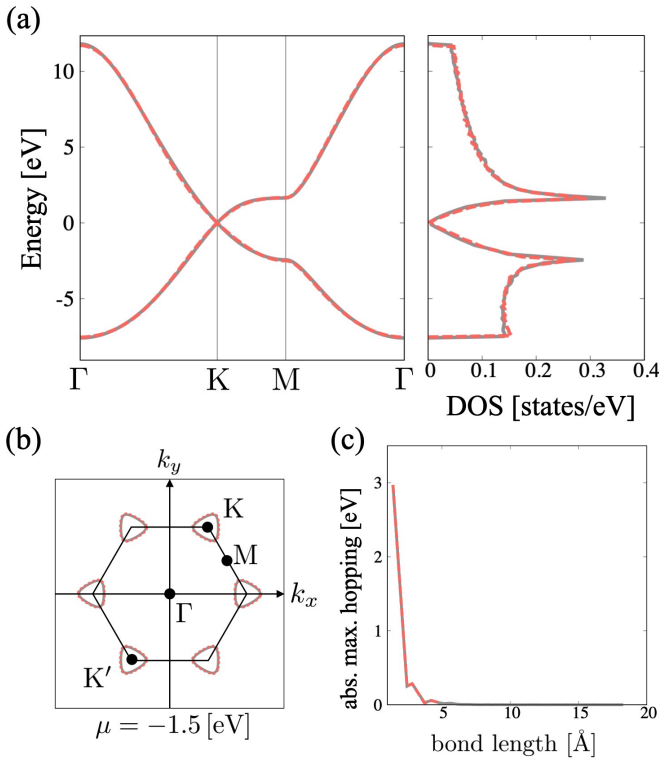
FIG. 8. (a) Comparison of the energy dispersion and DOS for the optimized SAMB TB with $N_{\max}^{(b)} = 6$. (b) The isoenergy surface at $\mu = -1.5$ eV. (c) The bond length dependence of the maximum strength of hoppings. The gray solid (red dashed) lines represent the results of the DF Wannier (SAMB) TB model.

monolayer MoS_2. We show the results for the latter two materials in Supplemental Material.

IV. SUMMARY

In this paper, we have developed a symmetry-adapted modeling procedure for molecules and crystals. By constructing the SAMB for atomic ($\mathbb{X}_{l\xi,sk}$) and molecular/crystal structural ($\mathbb{Y}_{l\xi}$) parts separately in terms of point-group harmonics, we express the final SAMBs denoted by $\hat{\mathbb{Z}}_{l\xi,sk}$ or $\hat{\mathbb{Z}}_{l\xi,sk}(\boldsymbol{k})$ as the irreducible decomposition of these products. Since these SAMBs constitute a complete orthonormal basis set, they can describe any of electronic degrees of freedom in isolated cluster systems and periodic crystals. Once we obtain the

complete set of SAMBs, a physical system can be expressed in linear combination of these bases belonging to the identity irreducible representation of the system. Moreover, the SAMBs other than the identity irreducible representations are all the candidates of possible order parameters, for which emergent macroscopic physical properties are easily predicted as they are already classified by the irreducible representation of the point-group symmetry.

We have demonstrated our method to electronic modeling of graphene as the simplest example, where the modeling parameters (linear coefficients of each SAMB) are optimized so as to reproduce the electronic structures given by the density-functional computation. As compared with *de facto* standard method of Wannier tight-binding modeling, the model obtained by our method satisfies rigorously the symmetry of the system, in which we can freely choose a range of hoppings. This aspect is a strong advantage to compactify the relevant model to discuss various response functions and many-body effects with low computational cost. Furthermore, meaning of physical operators is apparent since we describe any of atomic degrees of freedom in terms of atomic-orbital Hilbert space.

Although we have demonstrated our method only to electronic tight-binding modeling, our modeling procedure can also be utilized to decompose two-body multipolar interactions, including the density-density one, magnetic exchange couplings including Dzyaloshinskii-Moriya type [33–35], and mechanical lattice model expressing the dynamical matrix of phonon [36,37].

Since the present SAMBs all belong to the root spherical harmonics in rotation group, various systems can be compared quantitatively with each other via the weight of spherical harmonics. It is a crucial property of representation required for good descriptors in machine-learning-based materials design [38,39]. Therefore, the present method provides us with fundamental basis to develop symmetry-based analysis for materials science.

[1] P. Hohenberg and W. Kohn, Inhomogeneous electron gas, Phys. Rev. **136**, B864 (1964).

[2] W. Kohn and L. J. Sham, Self-consistent equations including exchange and correlation effects, Phys. Rev. **140**, A1133 (1965).

[3] R. G. Parr and Y. Weitao, *Density-Functional Theory of Atoms and Molecules* (Oxford University Press, New York, 1994)

[4] W. Koch and M. C. Holthausen, *A Chemist's Guide to Density Functional Theory, Second Edition* (Wiley, New York, 2001).

[5] R. M. Martin, *Electronic Structure: Basic Theory and Practical Methods* (Cambridge University Press, Cambridge, UK, 2004).

[6] N. Marzari, A. A. Mostofi, J. R. Yates, I. Souza, and D. Vanderbilt, Maximally localized Wannier functions: Theory and applications, Rev. Mod. Phys. **84**, 1419 (2012).

[7] A. A. Mostofi, J. R. Yates, Y.-S. Lee, I. Souza, D. Vanderbilt, and N. Marzari, wannier90: A tool for obtaining maximally-localised Wannier functions, Comput. Phys. Commun. **178**, 685 (2008).

[8] A. A. Mostofi, J. R. Yates, G. Pizzi, Y.-S. Lee, I. Souza, D. Vanderbilt, and N. Marzari, An updated version of wannier90: A tool for obtaining maximally-localised Wannier functions, Comput. Phys. Commun. **185**, 2309 (2014).

[9] G. Pizzi, V. Vitale, R. Arita, S. Blügel, F. Freimuth, G. Géranton, M. Gibertini, D. Gresch, C. Johnson, T. Koretsune *et al.*, Wannier90 as a community code: new features and applications, J. Phys.: Condens. Matter **32**, 165902 (2020).

[10] F. Neumann and O. Meyer, *Vorlesungen über die Theorie der Elasticität der Festen Körper und des Lichtäthers: Gehalten an der Universität Königsberg*, Franz Neumann No. 5 (B. G. Teubner, 1885).

[11] L. D. Landau, On the theory of phase transitions. i., Zh. Eksp. Teor. Fiz. **11**, 19 (1937).

[12] S. Hayami and H. Kusunose, Microscopic description of electric and magnetic toroidal multipoles in hybrid orbitals, J. Phys. Soc. Jpn. **87**, 033709 (2018).

[13] S. Hayami, M. Yatsushiro, Y. Yanagi, and H. Kusunose, Classification of atomic-scale multipoles under crystallographic point groups and application to linear response tensors, Phys. Rev. B **98**, 165110 (2018).

[14] S. Hayami, Y. Yanagi, and H. Kusunose, Bottom-up design of spin-split and reshaped electronic band structures in antiferromagnets without spin-orbit coupling: Procedure on the basis of augmented multipoles, Phys. Rev. B **102**, 144441 (2020).

[15] H. Kusunose, R. Oiwa, and S. Hayami, Complete multipole basis set for single-centered electron systems, J. Phys. Soc. Jpn. **89**, 104704 (2020).

[16] Y. LeCun, Y. Bengio, and G. Hinton, Deep learning, Nature (Lond.) **521**, 436 (2015).

[17] R. Sakuma, Symmetry-adapted Wannier functions in the maximal localization procedure, Phys. Rev. B **87**, 235109 (2013).

[18] T. Koretsune, Construction of maximally-localized Wannier functions using crystal symmetry, Comput. Phys. Commun. **285**, 108645 (2023).

[19] M. Nakhaee, S. A. Ketabi, and F. M. Peeters, Machine learning approach to constructing tight binding models for solids with application to BiTeCl, J. Appl. Phys. **128**, 215107 (2020).

[20] Z. Wang, S. Ye, H. Wang, J. He, Q. Huang, and S. Chang, Machine learning method for tight-binding Hamiltonian parameterization from ab-initio band structure, npj Comput. Mater. **7**, 11 (2021).

[21] See Supplemental Material at http://link.aps.org/supplemental/10.1103/PhysRevB.107.195118 for the detailed descriptions of the basis construction and optimization of $SrVO_3$ and MoS_2. The Supplemental Material also contains Refs. [7–9,31,32,40–42].

[22] H. Kusunose and S. Hayami, Generalization of microscopic multipoles and cross-correlated phenomena by their orderings, J. Phys.: Condens. Matter **34**, 464002 (2022).

[23] M.-T. Suzuki, T. Nomoto, R. Arita, Y. Yanagi, S. Hayami, and H. Kusunose, Multipole expansion for magnetic structures: A generation scheme for a symmetry-adapted orthonormal basis set in the crystallographic point group, Phys. Rev. B **99**, 174407 (2019).

[24] F. D. M. Haldane, Model for a Quantum Hall Effect without Landau Levels: Condensed-Matter Realization of the "Parity Anomaly", Phys. Rev. Lett. **61**, 2015 (1988).

[25] G. Liu, Z. Wang, and S.-S. Li, Spin-Hall effect in the generalized honeycomb lattice with Rashba spin–orbit interaction, Phys. Lett. A **373**, 2091 (2009).

[26] R. Oiwa and H. Kusunose, Rotation, Electric-Field Responses, and Absolute Enantioselection in Chiral Crystals, Phys. Rev. Lett. **129**, 116401 (2022).

[27] R. Oiwa and H. Kusunose, Systematic analysis method for nonlinear response tensors, J. Phys. Soc. Jpn. **91**, 014701 (2022).

[28] P. Giannozzi, S. Baroni, N. Bonini, M. Calandra, R. Car, C. Cavazzoni, D. Ceresoli, G. L. Chiarotti, M. Cococcioni, I. Dabo *et al.*, QUANTUM ESPRESSO: A modular and open-source software project for quantum simulations of materials, J. Phys.: Condens. Matter **21**, 395502 (2009).

[29] J. P. Perdew and A. Zunger, Self-interaction correction to density-functional approximations for many-electron systems, Phys. Rev. B **23**, 5048 (1981).

[30] D. E. Rumelhart, G. E. Hinton, and R. J. Williams, Learning representations by back-propagating errors, Nature (Lond.) **323**, 533 (1986).

[31] A. Paszke, S. Gross, F. Massa, A. Lerer, J. Bradbury, G. Chanan, T. Killeen, Z. Lin, N. Gimelshein, L. Antiga, A. Desmaison, A. Kopf, E. Yang, Z. DeVito, M. Raison, A. Tejani, S. Chilamkurthy, B. Steiner, L. Fang, J. Bai *et al.*, Pytorch: An imperative style, high-performancedeep learning library, Advances in Neural Information Processing Systems **32**, 8024 (2019).

[32] D. P. Kingma and L. J. Ba, Adam: A method for stochastic optimization, in *Proceedings of the 3rd International Conference on Learning Representations* (ICLR, San Diego, 2015).

[33] T. Matsumoto and S. Hayami, Nonreciprocal magnons due to symmetric anisotropic exchange interaction in honeycomb antiferromagnets, Phys. Rev. B **101**, 224419 (2020).

[34] T. Matsumoto and S. Hayami, Nonreciprocal magnon excitations by the Dzyaloshinskii-Moriya interaction on the basis of bond magnetic toroidal multipoles, Phys. Rev. B **104**, 134420 (2021).

[35] S. Hayami and T. Matsumoto, Essential model parameters for nonreciprocal magnons in multisublattice systems, Phys. Rev. B **105**, 014404 (2022).

[36] A. Togo, First-principles Phonon calculations with Phonopy and Phono3py, J. Phys. Soc. Jpn. **92**, 012001 (2023).

[37] H. Tsunetsugu and H. Kusunose, Theory of energy dispersion of chiral phonons, J. Phys. Soc. Jpn. **92**, 023601 (2023).

[38] A. P. Bartók, R. Kondor, and G. Csányi, On representing chemical environments, Phys. Rev. B **87**, 184115 (2013).

[39] M.-T. Suzuki, T. Nomoto, E. V. Morooka, Y. Yanagi, and H. Kusunose, High-performance descriptor for magnetic materials: accurate discrimination of magneticsymmetries, arXiv:2304.06282 [cond-mat.mtrl-sci].

[40] J. P. Perdew, A. Ruzsinszky, G. I. Csonka, O. A. Vydrov, G. E. Scuseria, L. A. Constantin, X. Zhou, and K. Burke, Restoring the Density-Gradient Expansion for Exchange in Solids and Surfaces, Phys. Rev. Lett. **100**, 136406 (2008).

[41] E. Cappelluti, R. Roldán, J. A. Silva-Guillén, P. Ordejón, and F. Guinea, Tight-binding model and direct-gap/indirect-gap transition in single-layer and multilayer MoS_2, Phys. Rev. B **88**, 075409 (2013).

[42] J. P. Perdew, K. Burke, and M. Ernzerhof, Generalized Gradient Approximation Made Simple, Phys. Rev. Lett. **77**, 3865 (1996).